# Nano- and Micro-scale Structures

**Session Organizers:** Slava KRYLOV (Tel Aviv Univ.), Alan ZEHNDER (Cornell Univ.)

**Plenary Lecture: Abstract, Slides and Video**
Nanomechanical resonators and nanofluidic systems
*Harold G. CRAIGHEAD (Cornell University)*

**Keynote Lecture**
An atomistic-continuum elastic rod model of carbon nanotubes
*Karthick CHANDRASEKER, Subrata MUKHERJEE* (Cornell University)*

A novel shift-loaded blister test to characterize the multi-scale mechanical properties and adhesion-delamination behaviors of biomembranes
*Scott E. JULIEN (Northeastern University), Kuo-Kang LIU (Keele University), Kai-tak WAN* (Northeastern University),*

Hybrid sensing procedure for mass and position detection with nano and macro resonant cantilevers
*Nicolae LOBONTIU* (University of Alaska Anchorage), Iulian LUPEA, Rob ILIC, Harold G. CRAIGHEAD (Cornell University)*

Stability analysis of a curved microbeam actuated by a distributed electrostatic force
*Slava KRYLOV* (Tel Aviv University), Bojan R. ILIC (Cornell University), David SCHREIBER, Shimon SERETENSKY (Tel Aviv University), Harold G. CRAIGHEAD (Cornell University)*

**Keynote Lecture**
On the accuracy of compliant mechanical MEMS/NEMS lumped-parameter modeling
*Nicolae LOBONTIU (University of Alaska Anchorage)*

The response of a cantilever microbeam with a plate attached to its tip to mechanical shock
*Hassen OUAKAD (Binghamton University), Haider N. ARAFAT (Cessna Aircraft Company), Mohammad I. YOUNIS* (Binghamton University)*

Switch triggered by mass threshold
*Mohammad I. YOUNIS*, Fadi M. AL SALEEM (Binghamton University)*

Adhesion of freestanding beams and its application to micro- and nano-structures
*Kai-tak WAN (Northeastern University)*

Modeling and dynamics of coupled dome-shaped micromechanical oscillators
*Tuhin SAHAI, Alan ZEHNDER* (Cornell University)*

Fully Lagrangian dynamics of thin MEMS beam
*Ranajay GHOSH*, Subrata MUKHERJEE (Cornell University)*

For multiple-author papers:
Contact author designated by *
Presenting author designated by underscore

Proceedings of the 6th International Conference on
Computation of Shell and Spatial Structures
IASS-IACM 2008: "Spanning Nano to Mega"
28-31 May 2008, Cornell University, Ithaca, NY, USA
John F. ABEL and J. Robert COOKE (eds.)

# Nanomechanical resonators and nanofluidic systems

Harold G. CRAIGHEAD*

*Charles W. Lake, Jr. Professor of Engineering
Professor of Applied and Engineering Physics
Director, Nanobiotechnology Center
Cornell University
hgc1@cornell.edu

**Abstract**

We have explored the properties and applications of small-scale mechanical resonators and fluidic devices. Studied systems include lithographically defined structures in a range of geometries, including nanotubes, nanostrings, and membranes as thin as a single sheet of carbon. While we have employed a variety of mechanical actuation techniques, we have found that optical methods for both actuation and motion transduction have proven remarkably robust and applicable to even the smallest resonant structures. With larger dimensioned structures we have examined some of the practical issues of detection of particulate binding and detachment using resonant motion. Nanofluidic systems have been used for single molecule analysis and controlling the confirmation and position of individual DNA molecules. The fabrication, properties and applications of these systems as sensors and analytical devices will be discussed.

Proceedings of the 6th International Conference on
Computation of Shell and Spatial Structures
IASS-IACM 2008: "Spanning Nano to Mega"
28-31 May 2008, Cornell University, Ithaca, NY, USA
John F. ABEL and J. Robert COOKE (eds.)

# An atomistic-continuum elastic rod model of carbon nanotubes

Karthick CHANDRASEKER, Subrata MUKHERJEE*

*Cornell University
220 Kimball Hall, Ithaca, NY 14853.
sm85@cornell.edu

## Abstract

The present work focuses on an atomistic-continuum model of single-walled carbon nanotubes (SWNTs) based on an elastic rod theory (Healey [1]) which can exhibit geometric as well as material nonlinearity. In particular, the SWNT is modeled as a one-dimensional elastic continuum which has some finite thickness bounded by the lateral surface. Exploitation of certain symmetries in the underlying atomic structure leads to suitable representations of the continuum elastic energy (Healey [1]). The bridging between the atomic scale and the effective continuum is carried out by parameterization of the continuum elastic energy and determination of the parameters using atomistic simulations.

## 1. Introduction

Continuum elastic behavior of SWNTs has often been characterized using properties such as Young's and shear moduli. These linearized measures adequately describe material behavior under small strains. However, in SWNTs undergoing large strains, there are effects such as the coupling between extension and twist (Chandraseker and Mukherjee [2]) which are not captured by linearized, isotropic moduli. While this is an evidence of anisotropy in large strains, it is of interest to also characterize other deformation couplings in SWNTs. The following are the key contributions of the present work:

- The proposed rod model for SWNTs in this work takes into account: (a) bending (b) twist (c) shear (d) extension (e) coupled extension and twist, and (f) coupled bending and shears. Published work on elastic moduli has taken into account (a)-(d) individually for small strains, and past work (including Chandraseker and Mukherjee [2]) has considered (e). But this is the first effort at a unified large strain approach that takes into account all of these modes for SWNTs.
- While two-dimensional membrane models of SWNTs (e.g., Chandraseker and Mukherjee [2]; Arroyo and Belytschko [3]) have been useful to predict localized effects such as buckled mode shapes of the effective continuum, they may not be computationally efficient to model global behavior of long tubes (microns in length) of interest in nano-oscillators (see, for e.g. Sazonova *et al.* [4]; Ustunel *et al.* [5]). A one-dimensional model is better suited to such an application. However, one-dimensional models published so far are limited to linear stress-strain relationships with isotropic material assumptions which do not take into account the aforementioned couplings.
- Finally, since this is a parameterized continuum model of an atomic system, it is possible to apply this model, by suitable parameter estimation, to other atomic systems such as silicon or boron nitride nanotubes.

## 2. Special Cosserat rod: Basic kinematics and constitutive model

It is assumed that the reference configuration of the rod is straight with a prismatic cross-section and that plane sections remain plane after deformation. (Rods that are initially bent - a common situation in practice - can be modeled by extending the theory presented below). Referring to Figure 1, one has:

$$\mathbf{x} = \mathbf{f}(\mathbf{X}) = \mathbf{r}(s,t) + X_\alpha \mathbf{d}_\alpha(s,t)$$
$$\text{with} \quad \mathbf{X} = X_\alpha \mathbf{e}_\alpha + s\mathbf{e}_3 \qquad \text{Here} \quad s = X_3 \tag{1}$$

In the above, **X** and **x** are undeformed and deformed coordinates, respectively, s = $X_3$ is the arc length in the reference configuration, $t$ is time, **r** is the position vector of a point on the rod centerline in the deformed configuration, $\mathbf{e}_\alpha$ are Cartesian unit vectors and $\mathbf{d}_\alpha$ are director vectors that span the cross-section (assumed to be planar). Summation is implied on all repeated indices and the range of Greek indices such as $\alpha$ is 1, 2.

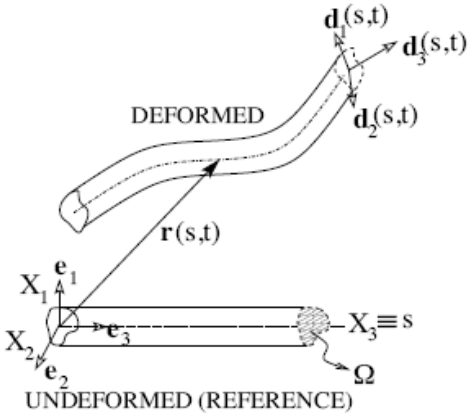


Figure 1: Cosserat rod notation

A special Cosserat theory is employed in which:

$$\mathbf{d}_i \cdot \mathbf{d}_j = \delta_{ij}, \quad \mathbf{d}_3 = \mathbf{d}_1 \times \mathbf{d}_2, \quad \mathbf{d}_i(s,t) = \mathbf{R}(s,t)\mathbf{e}_i, \quad i = 1,2,3 \tag{2}$$

where: $\delta_{ij}$ are the components of the Kronecker delta and the matrix **R** represents the rotation of the cross-section of the rod. Based on the above kinematic description, one can define strains as follows:

$$\mathbf{r}_{,s}(s,t) = \nu_i \mathbf{d}_i(s,t) \tag{3}$$

where: $\nu_1$, $\nu_2$ are shear strains, and $\nu_3$ is the axial stretch (axial strain = $\nu_3$-1).

Further,

$$\mathbf{d}_{i,s}(s,t) = \mathbf{R}_{,s}(s,t)\mathbf{e}_i = \mathbf{R}_{,s}\mathbf{R}^T\mathbf{d}_i$$
$$\equiv \mathbf{K}\mathbf{d}_i(s,t) = \boldsymbol{\kappa} \times \mathbf{d}_i(s,t) \tag{4}$$

where: $\kappa_1$, $\kappa_2$ are measures of the bending curvatures, and $\kappa_3$ is a measure of the twist.

It can be shown that the most general quadratic representation of the strain energy density for hemitropic, flip symmetric rods (see Healey [1] for definitions and details) is of the form:

$$W = \frac{1}{2}\left[ A\,\kappa_\alpha\kappa_\alpha + B\,\kappa_3^{\,2} + C\,\nu_\alpha\nu_\alpha + D\left(\nu_3 - 1\right)^2 + 2E\left(\nu_3 - 1\right)\kappa_3 + 2F\,\nu_\alpha\kappa_\alpha \right] \tag{5}$$

where $\int_0^L W\,ds$ gives the total elastic energy stored in a rod of undeformed length 'L' for a given deformation specified by $\nu_i$, $k_i$ (i = 1, 2, 3). The parameters 'A' through 'F' are coupling coefficients and represent the different coupling effects in bending, shear, extension and twist of the rod. For example, the coefficient 'E' represents the extension-twist coupling which has been studied previously (see, for e.g., Chandraseker and Mukherjee [2]).

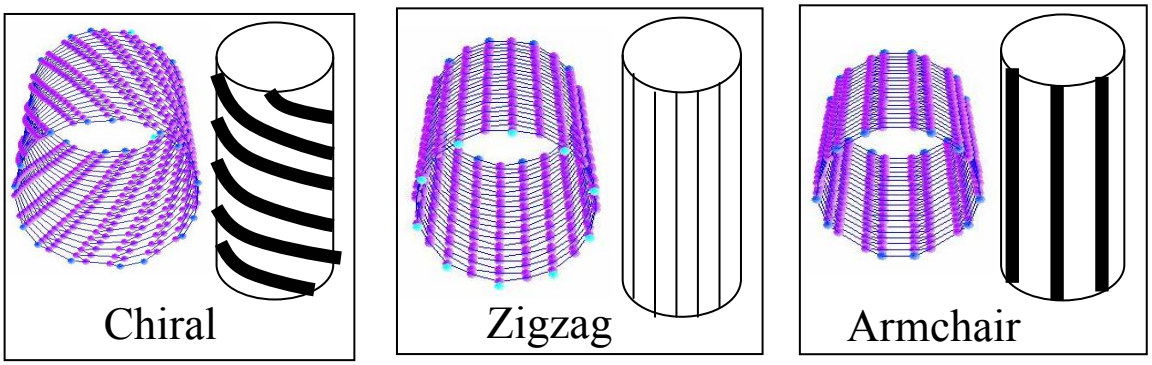


Figure 2: Helical idealizations of single-walled carbon nanotubes

### 2.1 Helical symmetry

SWNTs can be shown to possess a helical atomic arrangement as illustrated in Figure 2 (zigzag and armchair SWNTs can be modeled as special cases of this helical atomic arrangement with zero helical pitch).

It is observed that rods possessing a single-helical structure exhibit a special flip symmetry (180-degree rotation invariance) about a unique axis passing through the intersection of the helix with a plane perpendicular to the rod axis (as illustrated in Figure 3) at any point along the axis. This symmetry axis "rotates" as we move from cross-section to cross-section along the length of the rod (see Figure 3).

Further, in the case of chiral nanotubes, the atomic arrangement can be viewed as comprising of multiple helices (see Figure 2). In this case, there exist two or more equally spaced symmetry axes (see Figure 3). Consequently, it can be shown (Healey [1]) that for rods exhibiting n-fold multiple helical symmetry with $n \geq 3$ (which is true for any realistic chiral nanotube), the most general *quadratic* strain energy density is identical to the case of hemitropy + flip symmetry, i.e. the strain energy density function up to quadratic order is the same as Eq. (5). Since armchair and zigzag nanotubes can be treated as zero-pitch helices, the above description also applies to such nanotubes.

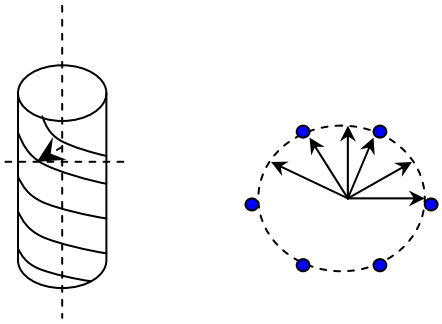

Figure 3: Single and multiple (for n = 6) helical symmetries

Hence, a continuum SWNT rod model up to quadratic order is immediately realized once the parameters 'A' through 'F' in Eq. (5) can be evaluated for SWNTs.

## 3. Summary

In order to extract the coefficients 'A' through 'F', unit cell simulations of extension, twist, bending and shear deformations are performed using a self-consistent-charge density-functional-tight-binding approach (see, for e.g., Frauenheim *et al.* [6]). The strain measures for the rod model are extracted using the atom locations to define cross-sections for the rod model. Using the extracted strains and the relaxed cell energies, the coefficients in Eq. (5) are evaluated through a least-squares fitting procedure. The key results from simulations on a (9,6) SWNT are:

- The quadratic extension-twist coupling coefficient 'E' can be shown to be zero.
- The shear modulus (a measure of stiffness to rotations of cross-sections about axes in-plane) can be shown to be one-fifth of the twist modulus indicating that the SWNT is five times stiffer in twist compared to shear.
- The bending stiffness can be shown to be one-tenth of a Bernoulli-Euler beam prediction indicating that direct application of a continuum beam model to SWNTs can significantly overestimate the bending stiffness.

## Acknowledgement

The collaboration with Dr. Jeffrey T. Paci and Prof. George C. Schatz at Northwestern University is gratefully acknowledged.

## References

[1] Healey TJ. Material symmetry and chirality in nonlinearly elastic rods. *Math. Mech. of Solids* 2002; **7**: 405-420.

[2] Chandraseker K and Mukherjee S. Atomistic-continuum and *ab initio* estimation of the elastic moduli of single-walled carbon nanotubes. *Comp. Mat. Sci.* 2007; **40(1)**: 147-158.

[3] Arroyo M and Belytschko T. Finite element methods for the non-linear mechanics of crystalline sheets and nanotubes. *Int. J. Numer. Meth. Engineering* 2004; **59**: 419–456.

[4] Sazonova V, Yaish Y, Üstünel H, Roundy D, Arias TA, McEuen PL. A tunable carbon nanotube electromechanical oscillator. *Nature* 2004; **431**: 284-287.

[5] Üstünel H, Roundy D, Arias TA. Modeling a suspended nanotube oscillator. *Nanoletters* 2005; **5(3)**: 523-526.

[6] Frauenheim T, Seifert G, Elstner M, Niehaus T, Köhler C, Amkreutz M, Sternberg M, Hajnal Z, Di Carlo A, Suhai S. Atomistic simulations of complex materials: ground-state and excited-state properties. *J. Phys.: Condens. Matter* 2002; **14**: 3015-3047.

Proceedings of the 6th International Conference on
Computation of Shell and Spatial Structures
IASS-IACM 2008: "Spanning Nano to Mega"
28-31 May 2008, Cornell University, Ithaca, NY, USA
John F. ABEL and J. Robert COOKE (eds.)

# A novel shaft-loaded blister test to characterize the multi-scale mechanical properties and adhesion-delamination behaviors of thin membranes

Scott E. JULIEN [1], Kuo-Kang LIU [2], Kai-tak WAN [1,*]

[1] Mechanical and Industrial Engineering, Northeastern University, Huntington Ave, Boston, MA 02115
[2] Institute of Science and Technology in Medicine, School of Medicine, Keele University, Stoke-on-Trent, ST4 7QB United Kingdom
* Corresponding author, ktwan@coe.neu.edu

## Abstract

A novel shaft-loaded blister test is designed to measure the elastic and viscoelastic materials parameters of a clamped circular membrane using an external (i) a quasi-static and (ii) static load. The new method is the only viable way for long term creep test with zero mechanical drift, and is therefore appealing in characterizing ultra-thin membranes. The governing elastic equation can be modified to account for local adhesion-delamination between a clamped film and a rigid substrate. The magnitude and range of the intersurface forces are allowed to vary. Computational results show the transition from classical Johnson-Kendall-Roberts (JKR) limit with infinite magnitude and Derjagiun-Muller-Toporov (DMT) limit with infinite range. The model is particularly useful in quantifying specific and non-specific surface interactions in thin biomembranes and single cells.

## 1. Introduction

Ultra-thin membranes can be mechanically characterized by clamping the sample between two washers or O-rings to form a freestanding diaphragm while applying an external load in the center (Fig.1). Depending on the dimension of the hole bored in the clamping plates, the simple testing configuration allows the specimen dimension to span multi-scale [1]. The new method supersedes the conventional ASTM that requires a delicate membrane to be clamped by gigantic fixtures. Standard universal testing machine or micro-force tester with quasi-static and cyclic loading capability can be used to simultaneously measure the applied load as a function of central displacement and thus yields the elastic and viscoelastic materials parameters of the sample. Static loading with absolutely zero mechanical and thermal drifts can be achieved by leaving a ball bearing of fixed weight sitting on the membrane center. The method can also be adapted to measure interfacial adhesion between a clamped membrane and a rigid substrate or yet another similar or dissimilar film.

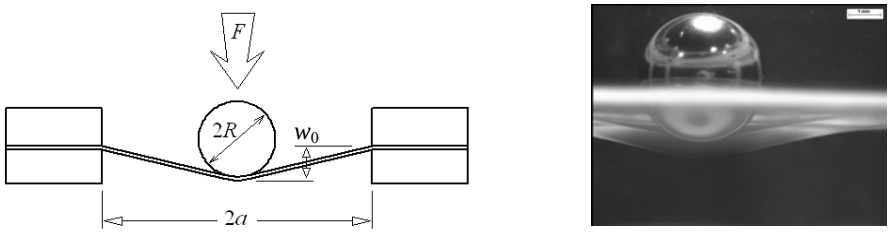


Fig.1. A circular clamped membrane is loaded by either the weight of a ball bearing (static) or a spherical capped cylindrical shaft. A hydrogel for prosthetic cornea construct is showed [2].

## 2. Theoretical model

A thin membrane with thickness, $h$, transverse elastic modulus across the film thickness, $E_t$, planar elastic modulus, $E$, Poisson's ratio, $\nu$, and a bending rigidity defined to be $\kappa = Eh^3/12(1-\nu^2)$ is clamped at the perimeter by two washers of radius, $a$. The external force, $F$, is applied to the center via a ball bearing (or a rounded shaft) with radius, $R$, resulting in a central displacement, $w_0$. Simultaneous measurement of $F$, $w_0$, and $c$ yields the materials properties $E_t$ and $E$. Depending on the magnitude of $F$, $w_0$ spans multi-scale from $R$ to many times of $h$.

### 2.1 Multi-scale mechanical characterization of thin membrane

Figure 2 shows a thin film with thickness, $h$, transverse elastic modulus across the film thickness, $E_t$, planar elastic modulus, $E$, Poisson's ratio, $\nu$, and a bending rigidity defined to be $\kappa = Eh^3/12(1-\nu^2)$. The film is clamped at the perimeter by two identical rigid rings of radius, $a$. An external mechanical force, $F$, is applied to the film center via a spherical capped shaft (or a ball bearing of a specific weight) with radius, $R$, leading to a central displacement, $w_0$. Simultaneous measurement of $F$ and $w_0$ allows $E_t$ and $E$ to be deduced. Depending on the ranges of $F$, $w_0$ spans multi-scale from $R$ to many times of $h$. Assuming $R << a$, superposition requires

$$w_0 = \underbrace{\left(\frac{9}{16R}\right)^{1/3}\left(\frac{1-\nu^2}{E_t}\right)^{2/3}F^{2/3}}_{\text{Hertz Indentation}} + \underbrace{\frac{3a^2}{4\pi\, h^3}\left(\frac{1-\nu^2}{E}\right)F}_{\text{Plate Bending}} + \underbrace{\left(\frac{4a^2}{\pi\, h}\right)^{1/3}\left(\frac{1-\nu^2}{E}\right)^{1/3}F^{1/3}}_{\text{Membrane Stretching}} \quad (1)$$

The deformation process takes consecutive modes. As $F$ increases from null, the micro-scale ($w_0 \sim R$) Hertz indentation dominates with $F \propto w_0^{3/2}$, then the meso-scale ($w_0 < h$) plate-bending with $F \propto w_0$, followed by a bending-stretching transition, and finally the macro-scale ($w_0 > h$) membrane-stretching with $F \propto w_0^3$. A parameter $\lambda = F\, a^2 / \kappa\, h$ is defined to gauge the dominant deformation mode. Bending-stretching transition occurs in the range $85 < \lambda < 30000$. Tensile residual membrane stress can be introduced to the model but is not discussed here. Figure 2 shows the multi-scale behavior. Viscoelastic membrane can be characterized in terms of $E'$, $E''$, and tanδ using the same testing configuration but under cyclic loading.

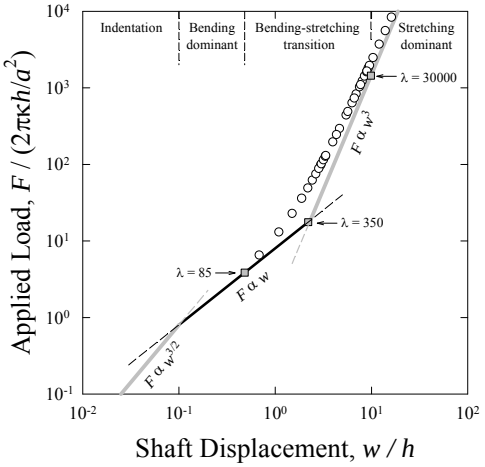


Fig. 2. The multi-scale behavior of a clamped membrane loaded at the center, showing the transition from indentation, plate-bending, mixed bending-stretching and membrane stretching. The data points are generated by finite element analysis.

### 2.2 Adhesion-delamination mechanics

Figure 3 shows a modified configuration for adhesion measurement. A cylindrical punch with a planar surface makes adhesive contact with the clamped membrane. Tensile force applied to the punch shrinks the contact radius to $c$ (< $a$). Deformed profile of the annulus is governed by the von Karman equation [3]

$$\kappa \nabla^4 w - \sigma h \nabla^2 w = F\, \delta(r) \quad (3)$$

with σ the membrane stress due to deformation. To allow the membrane to delaminate from the substrate, the Dugdale-Barenblatt-Maugis cohesive zone approximation is adopted here. The disjoining pressure is given by a constant magnitude, ρ, extends over a finite range, α. The Johnson-Kendall-Roberts (JKR) limit requires the force law to assume a delta function with an infinite magnitude but zero range, while the Derjaguin-Muller-Toporov (DMT) assumes a Heaviside step function with zero magnitude but infinite range. The delamination mechanics is derived here for freestanding membranes by establishing a simple energy balance

$$\frac{\partial}{\partial(\pi c^2)}\left(F.w_0 - \int F.dw_0 - \pi c^2\gamma\right) = 0 \tag{4}$$

where the three bracketed terms correspond to the potential energy of the external load, elastic energy stroed in the freestanding annulus, and surface energy to create new surfaces, respectively. The constitutive relation relating $F$, $w_0$, $c$) can thus be derived in terms of the adhesion energy, γ.

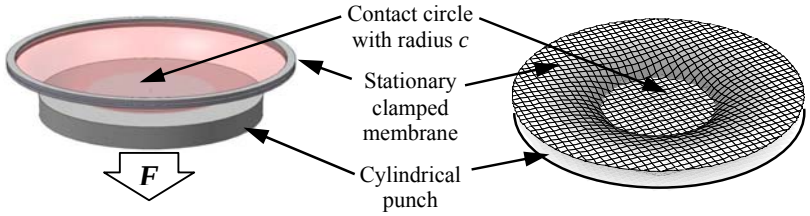


Fig. 3. External load applied to the punch drives a circular delamination.

Figure 4 shows the predicted delamination process for a linear elastic, thin and flexible membrane with κ = 0, fixed γ, and a range of surface force magnitude. In the JKR limit, as $F$ (or the normalized quantity ϕ in Figure 4) increases from null, no delamination is seen until $F$ reaches a maximum. As the punch moves further, the contact circle shrinks and $F$ decreases. When the punch moves to the terminal value along this energy curve, the contact is radius is reduced to $c^*$, where $(\partial w_0/\partial F)_{r=c^*} = 0$. Further incremental increase in $w_0$ leads to "pull-off", i.e. spontaneous detachment of film from punch. Keeping the same γ but varying the surface force magnitude, the delamination mechanics deviates from the JKR limit as shown. In the DMT limit, the overhanging annulus is always under the influence of surface forces at any external force. Here, however, $F$ is a monotonic increasing function of $w_0$. The dashed curve traces the "pull-off". The mechanical response allows the adhesion energy to be deduced.

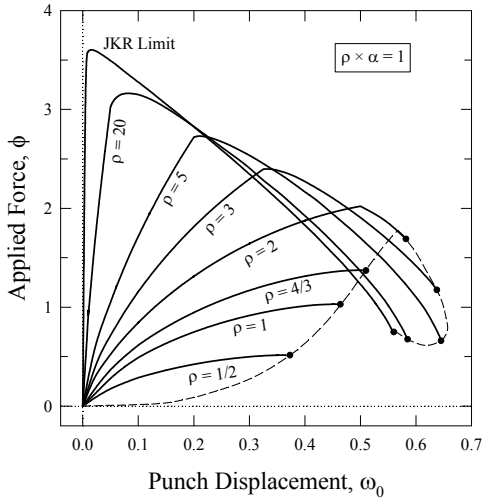


Fig. 4. Delamination trajectory for a fixed adhesion energy, γ = 1 but with a range of magnitude and range of surface forces. Note the difference between the JKR limit as shown and the DMT limit (small ρ).

## 3. Discussion and Conclusion

The testing configuration is capable of characterizing (i) mechanical behavior of the sample membrane, (ii) the adhesion energy of the membrane-substrate interface, (iii) the adhesion-delamination trajectory, and (iv) the magnitude and range of the long-range intersurface force. The method is useful in characterizing membrane walls of biological cells and biomimetic microcapsules (e.g. drug delivery vesicles), single and multi-cell layered biomembranes, MEMS-RF-switch, micro-pumps, micro-actuators, and polymer membranes [4-5].

## Acknowledgement

Funding for this work by US National Science Foundation CMMI # 0757140 and CMMI # 0757138 is kindly acknowledged.

## References

[1] Liu KK and Wan KT. Multi-scale mechanical characterization of a freestanding polymer film using indentation. *International Journal of Materials Research* 2008; in press.

[2] Ahearne M, Yang Y, Then KY and Liu KK. An Indentation Technique to Characterize the Mechanical and Viscoelastic Properties of Human and Porcine Corneas. *Annals of Biomedical Engineering* 2007; DOI: 10.1007/s10439-007-9323-9.

[3] Wong MF, Duan G and Wan KT. Adhesion-delamination mechanics of a pre-stressed circular film adhered onto a rigid substrate. *Journal of Adhesion* 2007; 83: 67-83.

[4] Ju BF, Liu KK, Wong MF and Wan KT. A novel punch method to characterize interfacial adhesion and residual stress of a thin polymer film. *Engineering Fracture Mechanics* 2007; 74: 1101-1106.

[5] Raegen AN, Dalnoki-Veress K, Wan KT and Jones RAL. Measurement of adhesion energies and Young's modulus in thin polymer films using a novel axi-symmetric peel test geometry. *European Physical Journal E* 2006; 19: 453-459.

Proceedings of the 6th International Conference on
Computation of Shell and Spatial Structures
IASS-IACM 2008: "Spanning Nano to Mega"
28-31 May 2008, Cornell University, Ithaca, NY, USA
John F. ABEL and J. Robert COOKE (eds.)

# Hybrid sensing procedure for mass and position detection with nano and macro resonant cantilevers

Nicolae LOBONTIU*, Iulian LUPEA, Rob ILIC, Harold G. CRAIGHEAD

*University of Alaska Anchorage
3211 Providence Drive, Anchorage, AK 99508, USA
afnl@uaa.alaska.edu

## Abstract

A hybrid sensing procedure is presented, which combines analytical modeling and experimental testing of resonant multi-segment cantilevers in order to predict the amount and planar (x-y) position of external mass which deposits in a point-like fashion on these elastic structures. The three parameters which characterize the amount and position of the deposited mass can be determined by employing three equations of the modified (shifted) natural frequencies in torsion, out-of-plane bending and in-plane bending together with the in-situ, experimentally-available (real) natural frequencies. The cantilevers may comprise any number of geometrically-different segments that are serially connected, and actual results (based on experimental data recorded for both macro and nano specimens) are presented for a two-segment, circularly-notched configuration. The generic analytical model, which formulates the torsion and two bending natural frequencies for both the original cantilever and the one with the attached mass, is derived by means of Rayleigh's quotient approach, by taking into consideration stiffness and inertia properties from all cantilever segments. The connections between several non-dimensional geometric parameters, the original/shifted natural frequencies, and deposited mass amount and position are investigated through sensitivity analysis. Analytical model, finite element and experimental testing data corresponding to the natural frequencies in torsion, out-of-plane bending and in-plane bending corresponding to macro and nano two-segment, circularly-notched cantilever specimens are in agreement.

## 1. Introduction

This work analyzes the shift in the resonant response of cantilevers that are formed of several serially-connected segments when external matter attaches to the cantilever support. The amount and position of mass that attaches in a point-like manner to the segment that is located at the free end of the cantilever can be determined through this method. The natural frequencies decrease because of the mass increase; the resulting frequency shift can be measured experimentally or model-predicted. The main resonant motions that can be used to monitor the mass deposition process are out-of-plane bending, in-plane bending and torsion, as indicated in Fig. 1.

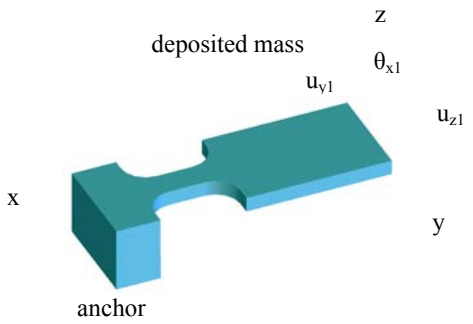


Figure 1: Cantilever with deposited point-like mass and main degrees of freedom

The principle of minute mass amounts detection through monitoring the resonant frequency shift of cantilevers has received a lot of attention lately in the field of MEMS/NEMS. Results of applying this method have been reported biological/medical investigations, chemical/physical analysis or hazardous substance detection – Raiteri *et al.* [15], Rogers *et al.* [16] or Pinnaduwage *et al.* [14]. The value of 2 x $10^{-7}$ that was suggested in the 1990s , Ward and Buttry [19], as the threshold of the frequency shift-to-natural frequency ratio in attached mass detection has been under constant challenge ever since as advances in nanofabrication and nano-detection enabled lowering the original limit. Particles have been detected with ever decreasing dimensions and masses, ranging from heavier viruses, Roman *et al.* [17] and lighter ones, Gupta *et al.* [3] or Ilic *et al.* [4], through single molecules of various substances, Luo [13] or Lavrik and Datskos [7], down to the level of single cell detection – Ilic *et al.* [5]. Masses at the level of attogram, Ilic *et al.* [6] and Li *et al.* [8], and even of zeptogram, Yang *et al.* [20] and Ekinci *et al.* [2], have been reported being resonantly detected. The modeling effort has mainly focused thus far on analytic procedures that addressed two-segment cantilevers and considered the root segment of a cantilever is compliant and massless whereas the paddle segment is rigid and possessing inertia, Ilic *et al.* [6] or Dufour and Fadel [1]. Improvements to this analytical model can be produced when considering that all cantilever segments possess both compliance and inertia properties, Lobontiu [9], Lobontiu *et al.* [10] or Sheeparamathy *et al.* [18].

## 2. Analytical model of generic n-segment cantilever

The Rayleigh's quotient method is utilized to derive the resonant frequencies corresponding to bending and torsional resonant motions. The resonant frequency shift in any of the three modes mentioned above enables quantifying and/or localizing the deposited mass. The model is a full-compliance (stiffness), full-inertia one in the sense that compliance and inertia contributions from all the segments are taken into consideration. The attached mass effect on inertia alteration is expressed in a weighted form, which is conducive to model accuracy improvement. Figure 2 illustrates the side and top view sketches of a cantilever that is made up of potentially *n* segments. A generic segment *i* of length $l_i$ is defined by a variable width $w_i$ that results from the geometric profile of the curve, which is assumed to be symmetric (mirrored) with respect to the longitudinal axis. All cantilever segments have the same thickness *t*.

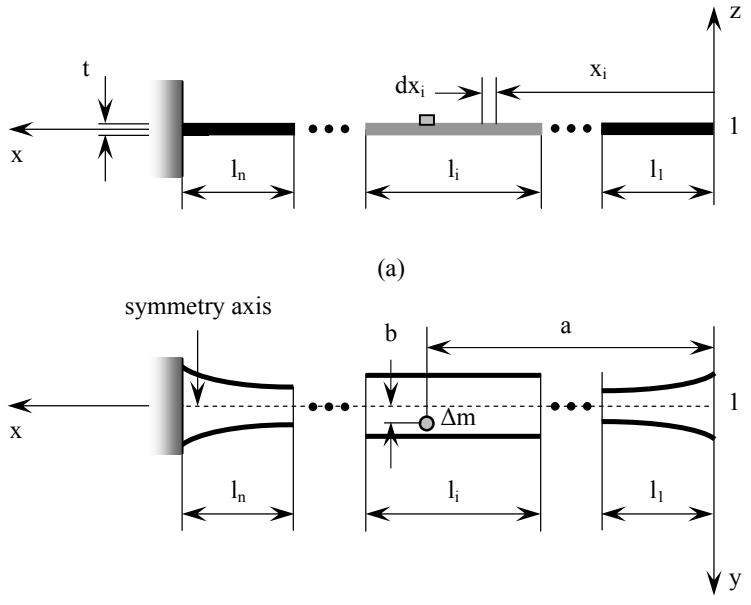


Figure 2. Main geometric parameters of symmetric, constant-thickness, multi-segment cantilever with offset deposited mass on an arbitrary segment: (a) side view; (b) top view

The *out-of-plane bending* resonant frequency is expressed according to Rayleigh's quotient method as:

$$\omega_{by,0}^2 = \frac{E\sum_{i=1}^{n}\left\{\int_{l_i} I_y(x_i)\left[\frac{d^2 f_b(x_i)}{dx_i^2}\right]^2 dx_i\right\}}{\rho\sum_{i=1}^{n}\left[\int_{l_i} A(x_i)\left[f_b(x_i)\right]^2 dx_i\right]} = \frac{k_{by}}{m_b} \tag{1}$$

where $k_{by}$ and $m_b$ are the equivalent (effective) stiffness and mass corresponding to bending about the y-axis. The simplified bending distribution function is:

$$f_b(x_i) = 1 - \frac{3}{2}\left(\frac{x_i}{\sum_{i=1}^{n} l_i}\right) + \frac{1}{2}\left(\frac{x_i}{\sum_{i=1}^{n} l_i}\right)^3 = 1 - \frac{3}{2}\left(\frac{x_i}{l}\right) + \frac{1}{2}\left(\frac{x_i}{l}\right)^3 \tag{2}$$

The errors introduced by using the approximate distribution function of Eq. (1) are in most of cases negligible – Lobontiu [12]. The effect of external matter $\Delta m$ attaching as a point mass on the first segment of the multiple-segment cantilever at a distance $a$ from the free end, is an increase in the total structural mass, which reduces the original bending resonant frequency to:

$$\omega_{by}^2 = \frac{k_{by}}{m_b + \left[f_b(a)\right]^2 \Delta m} = \frac{k_{by}}{m_b + \left[1 - \frac{3}{2}\left(\frac{a}{l}\right) + \frac{1}{2}\left(\frac{a}{l}\right)^3\right]^2 \Delta m} \tag{3}$$

For *in-plane bending*, the original and shifted resonant frequencies $\omega_{bz,0}^2$ and $\omega_{bz}^2$ can be expressed as in Eqs. (1) and (2), respectively, by simply using $I_z(x_i)$ instead of $I_y(x_i)$ because the bending distribution is the one of Eq. (4). In Eq. (5), $I_z(x_i) = [w(x_i)]^3 t / 12$ is the variable cross-sectional moment of inertia about the $z$-axis.

A similar procedure is followed to determine the original resonant frequency (see Lobontiu [12] for more details) as:

$$\omega_{t,0}^2 = \frac{G\sum_{i=1}^{n}\left\{\int_{l_i} I_t(x_i)\left[\frac{df_t(x_i)}{dx_i}\right]^2 dx_i\right\}}{\rho\sum_{i=1}^{n}\left[\int_{l_i} A(x_i)\frac{\left[w(x_i)\right]^2 + t^2}{12}\left[f_t(x_i)\right]^2 dx_i\right]} = \frac{k_t}{J_t} \tag{4}$$

The following distribution function can be utilized in Eq. (4):

$$f_t(x_i) = 1 - \frac{x_i}{\sum_{i=1}^{n} l_i} = 1 - \frac{x_i}{l} \tag{5}$$

and this is similar to the torsion distribution function of a constant cross-section cantilever, which is: $f_t(x) = 1 - x/l$. The torsion-related moment of inertia $I_t(x_i)$ depends on how the two cross-sectional dimensions, $w(x_i)$ and $t$. For *very thin cross-sections*, as the ones addressed in this report, the torsion moment of inertia is computed as: $I_t(x_i) = w(x_i)t^3/3$.

The torsion resonant frequency will alter when mass deposits by an offset quantity $b$ at a distance $a$ from the free end as:

$$\omega_t^2 = \frac{k_t}{J_t + b^2\left[f_t(a)\right]^2 \Delta m} = \frac{k_t}{J_t + b^2\left(1-\frac{a}{l}\right)^2 \Delta m} \tag{6}$$

## References


[1] Dufour I and Fadel V. Resonant microcantilever type chemical sensors: analytical modeling in view of optimization. *Sensors and Actuators B*; 2003; **91**:353-361.

[2] Ekinci KL, Yang YT, Roukes ML. Ultimate limits to inertial mass sensing based upon nanolectromechanical systems. *Journal of Applied Physics*; 2004; **95 (5)**: 2682-2689.

[3] Gupta A, Akim D, Bashir R. Single virus particle mass detection using microresonators with nanoscale thickness. *Journal of Applied Physics*; 2004; **84 (11)**: 1976-1978.

[4] Ilic B, Yang Y, Craighead HG. Virus detection using microelectromechanical devices. *Applied Physics Letters*; 2004; **85 (13)**: 2604-2606.

[5] Ilic B, Czaplewski D, Zalatudinov M, Craighead HG, Neuzil P, Campagnolo C, Batt C. Single cell detection with micromechanical oscillators. *Journal of Vacuum Science Technology*; 2001; **19(6)**: 2825-2828.

[6] Ilic B, Craighead HG, Krylov S, Senaratne W, Ober C, Neuzil P. Attogram detection using nanoelectromechanical oscillators. *Journal of Applied Physics*; 2004; **95 (7)**: 3694-3701.

[7] Lavrik N and Datskos P. Femtogram mass detection using photothermally actuated nanomechanical resonators. *Applied Physics Letters*; 2003; **82 (16)**: 2697-2699.

[8] Li M, Tang HX, Roukes ML. Ultra-sensitive NEMS-based cantilevers for sensing, scanned probe and very high-frequency applications. *Nature Nanotechnology*; 2007; **2**: 114-120.

[9] Lobontiu N. *Mechanical Microresonators: Modeling, Design, and Applications*, McGraw-Hill, New York, 2005.

[10] Lobontiu N, Ilic B, Garcia E, Reissman T, Craighead HG. Modeling of nanofabricated paddle bridges for resonant mass sensing. *Review of Scientific Instruments*; 2006; 77: 073301-1 - 073301-9.

[11] Lobontiu N and Garcia E. Two microcantilever designs: modeling for static deflection and modal analysis. *Journal of Microelectromechanical Systems*; 2004; **13(1)**: 41-50.

[12] Lobontiu N. *Dynamics of Microelectromechanical Systems*, Springer, New York, 2007.

[13] Luo C. Inaccuracy in the detection of molecules using two microcantilever-based methods. *Journal of Applied Mechanics*; 2005; **72**: 617-619.

[14] Pinnaduwage L, Boiadjiev V, Hawk JE, Thundat T. Sensitive detection of plastic explosives with self-assembled monolayer-coated microcantilevers. *Applied Physics Letters*; 2003; **83 (7)**: 1471-1473.

[15] Raiteri R, Grattarola M, Butt HJ, Skladal P. Micromechanical cantilever-based biosensors. *Sensors and Actuators B*; 2001; **79**: 115-126.

[16] Rogers B, Manning L, Jones M, Sulchik T, Murray K, Benneschott B, Adams JD, Hu Z, Thundat T, Cavazos H, Minne SC. Mercury vapor detection with a self-sensing resonating piezoelectric cantilever. *Review of Scientific Instruments*; 2003; **74 (11)**: 4899-4901.

[17] Roman C, Ciontu F, Courtois B. Single molecule detection and macromolecular weighting using an all-carbon-nanotube nanoelectromechanical sensor. *Proceedings of the 4th Conference on Nanotechnology*; 2004: 263-266.

[18] Sheeparamatti BG, Hebbal MS, Sheeparamatti RB, Math VB, Kadadevaramath JS. Simulation of biosensor using FEM. *Journal of Physics*; 2006; **34**: 241-246.

[19] Ward MD and Buttry DA. In-situ interfacial mass detection with piezoelectric transducers. *Science*; 1990; **249**: 1000-1007.

[20] Yang YT, Callegari C, Feng XL, Ekinci KL, Roukes ML. Zeptogram-scale nanomechanical mass sensing. *Nano Letters*; 2006; **6 (4)**: 583-586.

Proceedings of the 6th International Conference on
Computation of Shell and Spatial Structures
IASS-IACM 2008: "Spanning Nano to Mega"
28-31 May 2008, Cornell University, Ithaca, NY, USA
John F. ABEL and J. Robert COOKE (eds.)

# Stability analysis of a curved microbeam actuated by a distributed electrostatic force

Slava KRYLOV*, Bojan R. ILIC, David SCHREIBER, Shimon SERETENSKY, Harold G. CRAIGHEAD

*School of Mechanical Engineering, Faculty of Engineering, Tel Aviv University
Ramat Aviv 69978 Tel Aviv Israel
vadis@eng.tau.ac.il

## Abstract

We report on a theoretical and experimental stability investigation of an initially curved clamped-clamped microbeam actuated by a distributed electrostatic force. Reduced order Galerkin and consistently constructed lumped models of the shallow Euler-Bernoulli beam were built and verified by numerical analysis and the influence of various parameters on the stability was investigated. As a result of the interaction between mechanical and electrostatic nonlinearities the device may exhibit sequential snap-through buckling and pull-in instability and bistable behavior. The first critical voltage can be higher or lower than the second one while the stable deflections are significantly larger than in a straight beam. Due to influence of the nonlinear electrostatic force the minimal initial elevation required for the appearance of the snap-through instability is smaller than in the case of a uniform loading and depends on the distance between the beam and the electrode. The closed form approximation of this elevation was evaluated. The devices were fabricated from silicon on insulator (SOI) wafer using deep reactive ion etching and in-plane responses were characterized by means of optical and Scanning Electron microscopy. Model results obtained for the actual dimensions of the device were in good agreement with the experimental data.

## 1. Introduction

Pull-in instability of electrostatically actuated micro structures is encountered as a basic instability mechanism of this kind of devices (Pelesko and Bernstein [1]). If a mechanical constraint is provided limiting the displacement, an additional stable equilibrium may exist beyond the pull-in point and the system can be viewed as bistable. This "electrostatic bistability" is an intrinsic feature of electrostatic actuators and widely used in many micro devices. "Mechanical" snap-through instability arises due to the non-monotonous stiffness-deflection dependence of a structure and is accompanied by the bistability (e.g., see Simitses and Hodges [2]). In the present work we investigate the stability of a flexible initially curved micro beam with clamped ends actuated by a distributed electrostatic force. The structure is probably the simplest system combining both generic electrostatic nonlinearity as well as mechanical nonlinearity typical for bistable systems. The theoretical study of a curved electrostatically actuated beam was presented by Krylov *et al.* [3], this behavior was then confirmed experimentally by Krylov *et al.* [4]. Experimental observation of snap-through and pull-in instability in a curved beam was recently reported by Zhang *et al.* [5] but bistability was not demonstrated.

## 2. Model of a curved electrostatically actuated beam

### 2.1 Formulation and decomposition

We analyze a flexible initially curved double clamped prismatic micro beam of length $L$ with a rectangular cross-section of area $A$ and moment of inertia $I_y$ made of an isotropic linearly elastic material with the Young's modulus $E$ (since $b \gg \hat{d}$ we use a plain strain modulus $\tilde{E} = E\left(1-\nu^2\right)$ where $\nu$ is the Poisson's ratio). The beam is actuated by a distributed electrostatic force provided by an electrode located at the distance $g_0$ from the beam, fig.1 The initial shape of the beam is described by a function $\hat{h}z_0(\hat{x})$ such that $\max(z_0)=1$.

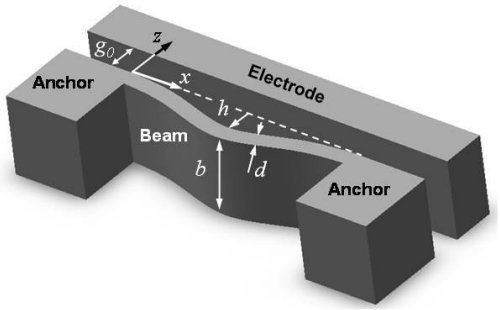


Figure 1: Electrostatically actuated curved beam.

Table 1: Non-dimensional quantities.

| | |
|---|---|
| $x = \hat{x}/L$ | Coordinate |
| $h = \hat{h}/g_0$ | Elevation |
| $d = \hat{d}/g_0$ | Thickness |
| $w = \hat{w}/g_0$ | Deflection |
| $\alpha = \left(g_0^2 A\right)/\left(2I_y\right)$ | Stretching parameter |
| $\lambda = \sqrt{L^2 A/I_y}$ | Slenderness |
| $\varepsilon = g_0/L$ | Aspect ratio |
| $\beta = \left(\varepsilon_0 b L^4 V^2\right)/\left(2\tilde{E}I_y {g_0}^3\right)$ | Voltage parameter |

The deflection $w(x)$ of the shallow Euler-Bernoulli beam is described by the non-dimensional equation

$$w^{IV} - \alpha\int_0^1 \left(2hz_0'w' - \left(w'\right)^2\right)dx\left(hz_0'' - w''\right) = \beta/\left(1 + hz_0 - w\right)^2 \tag{1}$$

completed by the boundary conditions $w = 0, \quad w' = 0$ at $x = 0$ and $x = 1$. Here $(\,)' = d/dx$. Non-dimensional quantities used in the formulation are presented in Table 1. We disregard at this stage the influence of fringing electrostatic fields and consider the electrostatic force in the framework of the parallel capacitor approach.

The deflection of the beam is approximated by the series

$$w(x) \approx \sum_{i=1}^{n} q_i \phi_i(x) \tag{2}$$

were $q_i$ are generalized coordinates and $\phi_i(x)$ are linear undamped eigenmodes of a straight beam normalized in such a way that $\max\left[\phi_i(x)\right] = 1$. Implementation of the Galerkin procedure yields the system of nonlinear coupled algebraic equations

$$\mathbf{Bq} + 2\alpha h^2 \mathbf{z}_0^T \mathbf{q} \mathbf{z}_0 - \alpha h \mathbf{q}^T \mathbf{S} \mathbf{q} \mathbf{z}_0 - 2\alpha h \mathbf{z}_0^T \mathbf{q} \mathbf{S} \mathbf{q} + \alpha \mathbf{q}^T \mathbf{S} \mathbf{q} \mathbf{S} \mathbf{q} = \beta \mathbf{F}_e \tag{3}$$

where $\mathbf{q} = \{q_i\}$ and elements of the vector $\mathbf{z}_0 = \{z_{0i}\}$, of the bending matrix $\mathbf{B} = \left[b_{ij}\right]$, of the stretch matrix $\mathbf{S} = \left[s_{ij}\right]$ and of the generalized force vector $\mathbf{F}_e = \{f_{ei}\}$ are

$$z_{0i} = \int_0^1 z_0' \phi_i' dx \quad b_{ij} = \delta_{ij} \int_0^1 \phi_i'' \phi_j'' dx \quad s_{ij} = \int_0^1 \phi_i' \phi_j' dx \quad f_{ei} = \int_0^1 \frac{\phi_i dx}{\left[1 + hz_0(x) - \sum_k q_k \phi_k(x)\right]^2} \tag{4}$$

The system (3) was solved numerically. In order to validate the RO model and investigate its convergence we compared the results provided by the RO model with the direct numerical solution of equation (1) based on the collocation method and obtained using the two-point Boundary-Value Problem integrated into the Matlab. In addition, we compare the results provided by the RO model with the data available in literature for the case of a uniform distributed force.

### 2.3 Model results

Using the RO model the influence of various parameters, mainly relative initial elevation $h$ and thickness $d$ was investigated. Results are presented in fig. 2. One observes that the bifurcation diagram may contain two maxima associated with the snap-through and pull-in instability as well as two branches corresponding to the stable equilibria. The voltage parameter corresponding to the snap-through buckling can be lower or higher

than the pull-in value while the maximal stable deflection corresponding to the secondary pull-in instability is larger than in the case of a straight beam. Both snap-through and pull-in values of the voltage parameter may be lower than $\beta_{PI}$ of the initially straight beam of the same geometry, fig. 2 (c).

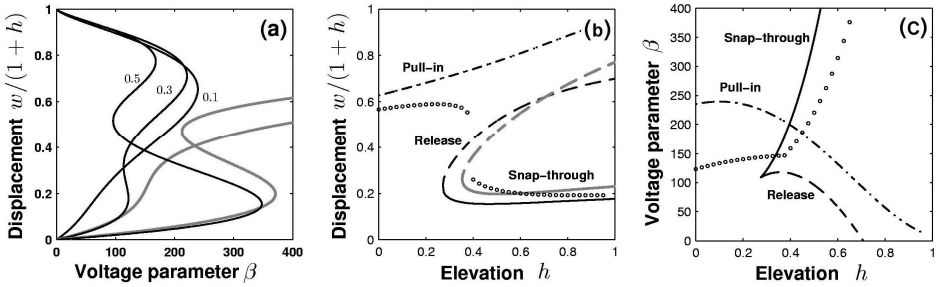


Figure 2: Bifurcation diagrams for varying initial elevations (a); critical values of relative displacements (b) and voltage parameter (c) for $\varepsilon = 0.01, d = 0.3$ and $d = 0.5$ (markers). Gray lines correspond to the case of uniform displacement independent force. The initial shape is $z_0(x) = \phi_1(x)$.

In order to exhibit snap-through buckling, the curvature of the beam should be higher than a certain value. Electrostatically actuated curved beams may exhibit the snap-through buckling at lower elevation/curvature and at smaller deflections than in the case of the uniform, deflection independent force. We preserve one term in eq. (2) and replace $\phi_1(x) = \left[1-\cos(2\pi x)\right]/2$ in the expressions for $f_e$ in eq. (4). In the case of a bell-shaped beam the system (3) is reduced to a single equation

$$\left(1+8\varepsilon^2 h^2 k\right) q_1 - 12\varepsilon^2 h k q_1^2 + 4\varepsilon^2 k q_1^3 = \frac{\beta}{2b_{11}\sqrt{\left(1+h-q_1\right)^3}} \tag{5}$$

describing the equilibrium of the electrostatically actuated shallow Mises truss, fig. 3(a) with $k = k_2/k_1 = \lambda^2 s_{11}^2/\left(8b_{11}^2\right) = 0.01498\lambda^2$ and modified electrostatic force given by the right hand side of eq. (5) . The stiffness of the vertical spring in fig. 3(a) is associated with the bending stiffness of the beam while the stiffness of the oblique springs is defined by the extensional stiffness and slenderness of the beam.

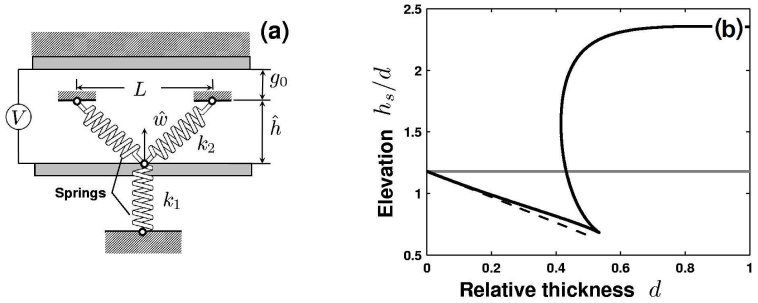


Figure 3: (a) Electrostatically actuated Mises truss. (b) Minimal relative initial elevation $h_S/d$ of a curved bell-shaped electrostatically actuated beam required for the snap-through instability to appear. The gray line corresponds to the case of a displacement independent force; dashed line corresponds to the approximation (5).

Using eq. (5), voltage parameter $\beta$ was calculated for prescribed deflection while critical values of $q_1$ and $\beta$ were found from the condition $d\beta/dq_1 = 0$. Requiring that the equation $d\beta/dq_1 = 0$ has three different real roots (in addition to $q_1 = 0$ and $q_1 = 1+h$), we obtain an expression relating the minimal snap-through value $h_S$ of the

initial elevation required for the existence of the snap-through buckling and parameters $\varepsilon$ and $k$, fig. 3(b). In the case $\hat{d}/g_0 \ll 1$ a simple approximation of $h_s$ is found

$$\frac{\hat{h}_s}{\hat{d}} \approx \frac{\hat{h}_0}{\hat{d}}\left[1-\frac{3}{4}\left(\frac{\hat{h}_0}{\hat{d}}\right)\frac{\hat{d}}{g_0}\right] \tag{6}$$

where $\hat{h}_0/\hat{d} = \sqrt{b_{11}/\left(6s_{11}^2\right)}$ corresponds to the case of uniform deflection independent loading. Our results suggest that the minimal values of the elevation required for the appearance of the snap-through buckling available in literature for the beams under uniform deflection independent loading cannot be directly used in the case of electrostatically actuated beams.

## 3. Experiment

The devices were fabricated of highly doped single crystal Si using SOI wafers as a starting material and etched using a deep reactive ion etching (DRIE) based process. The devices were operated in ambient air conditions as well as in vacuum inside a chamber of a scanning electron microscope (SEM). The beams were actuated by linearly increasing and decreasing voltages, the response of the beams was video-recorded and the voltage-displacement dependence was built using image processing. The pull-in behavior was in accordance with theoretical predictions. Comparison of experimental data with the results provided by the model (with the actual, measured, dimensions used in calculations) revealed very good agreement between the two.

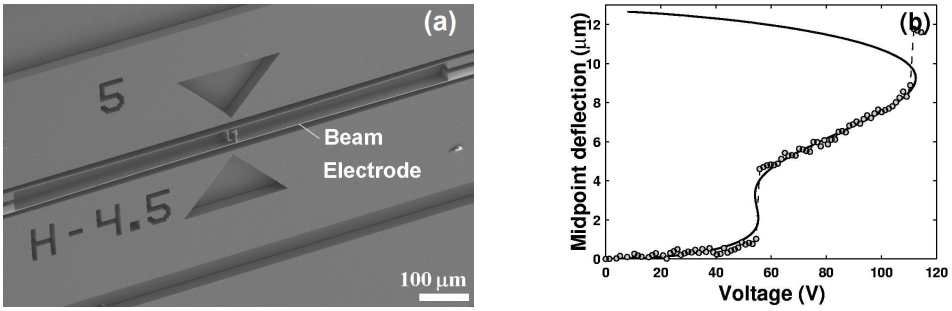


Figure 4: (a) Scanning Electron micrographs of the fabricated device. (b) Experimental bifurcation diagram (markers) for bell-shaped 1000 μm long beam for $h$ = 3 μm. Solid lines correspond to the model results for the 2.4 μm thick beam and distance to electrode $g_0$ = 10.1 μm measured using SEM.

## Acknowledgement

We would like to thank T. Shmilovich, Y. Borisenkov, A. Gurevich and the staff at the Tel Aviv University Micro-Fabrication Facility for aid in fabrication and L. Slepyan for fruitful discussions. This work was performed in part at the Cornell NanoScale Facility, a member of the National Nanotechnology Infrastructure Network, which is supported by the National Science Foundation (Grant ECS-0335765).

## References

[1] Pelesko J A and Bernstein D H. Modeling of MEMS and NEMS. Chapman&Hall A CRC Press Company, 2002.

[2] Simitses G J and Hodges D H. Fundamentals of Structural Stability. Elseiver, 2006.

[3] Krylov S and Seretensky S. Pull-in and multistability analysis of an initially curved beam, *Digest Tech. Papers APCOT 2006*, Singapore, June 25-28 2006, paper D-27.

[4] Krylov S, Seretensky S, Schreiber D. Pull-In behavior of electrostatically actuated multistable microstructures. *Proc. of the ASME 2007 IDETC&CIE Conference*, September 4-7, 2007, Las Vegas, Nevada, 2007, paper DETC2007-35552.

[5] Zhang Y, Wang Y, Li Z, Huang Y, Li D. Snap-through and pull-in instabilities of an arch shaped beam under an electrostatic loading *J. Microelectromech. Syst.* 2007; **16**: 684–693.

Proceedings of the 6th International Conference on
Computation of Shell and Spatial Structures
IASS-IACM 2008: "Spanning Nano to Mega"
28-31 May 2008, Cornell University, Ithaca, NY, USA
John F. ABEL and J. Robert COOKE (eds.)

# On the accuracy of compliant mechanical MEMS/NEMS lumped-parameter modeling

Nicolae LOBONTIU

University of Alaska Anchorage
3211 Providence Drive, Anchorage, AK 99508, USA
afnl@uaa.alaska.edu

## Abstract

Sensing/actuation micro and nano devices whose operation involves moving mechanical parts are largely based on monolithic, compliant mechanisms whereby the relative motion is produced through the elastic deformation of specially-designed flexible parts. The choice rationale of compliant MEMS/NEMS is twofold, being imposed by nanofabrication technology (which favors realization of monolithic, single-part products) and inherent virtues of the compliant structures (such as reductions in friction loss and hysteresis). On a coarse-to-fine modeling scale, where the finite element procedure tops the range with a host of capabilities, lumped-parameter methods are usually credited with the lowest prediction accuracy. However, such models are still needed, because they are generally based on closed-form equations, and are therefore almost indispensable in two domains, namely: first-hand, preliminary modeling/design (where fundamental relationships between design variables and performance criteria are needed) and input-output system control. As such, endeavors of refining lumped-parameter modeling techniques are underway in an attempt of balancing accuracy and computation costs. The paper discusses various methods that improve lumped-parameter modeling such as consideration of inertia and stiffness from all compliant members, utilization of real distribution functions that depend on specific geometry, consideration of shear-type deformation effects in the case of short members, as well as elastic properties modifications for deep members. A few nanocantilever designs are case-studied, and various precision models are generated, whose results are compared with finite element and experimental results.

## 1. Introduction

Compliant (or flexible) mechanical devices are largely utilized in micro/nano electromechanical systems (MEMS/NEMS) due to intrinsic advantages such as monolithic construction, robustness, compactness, no need for assembly or maintenance and to fabrication constraints such as planar design. While finite element methods are extremely useful in designing and numerically testing the performance of compliant MEMS/NEMS, they can be supplemented by lumped-parameter models, which (if developed with sufficient accuracy) can provide a fast and less expansive alternative into first-stage modeling. Moreover, control of MEMS/NEMS needs transfer functions connecting the input to the output, and the lumped-parameter models offer closed-form solutions that can be utilized as transfer functions.

Lumped-parameter procedures are based on simplifying assumptions whereby the actual distributed nature of mechanical components or systems is rendered into discrete (lumped) equivalent properties such as inertia, stiffness, damping or forcing, Ilic et al. [1], Lobontiu [2] and Lobontiu et al. [3]. Extreme simplifications to the real systems might generate lumped-parameter results which are approximate solutions, with accuracy levels that depend on the simplification depth. However, when sufficient care is paid to comply with the real physical constraints, lumped-parameter models are tools that generate precise results.

Cantilevers and bridges are two MEMS/NEMS mechanical device categories which are often times analyzed by employing lumped-parameter techniques before design refinements are brought in by means of finite element modeling. The quasi-static behavior of these devices is modeled by using the lumped stiffness, whereas their resonant response is qualified by also utilizing the lumped mass. A rule of thumb into modeling simplification

requires that bulkier parts of such a mechanical device, such as the paddle segment for instance be considered as rigid and bearing inertia, whereas thinner portions should be modeled as massless and flexible. This approach can prove sufficiently accurate, particularly when dimensional discrepancies between structural segments allow discriminating massive from tinnier parts, but when this separation becomes blurred due to dimensional similitude, lumped-parameters models that require consideration of inertia and stiffness from all segments are needed.

The paper analyzes a few cantilever and bridge examples that can be modeled by several layers of lumped-parameter modeling, and highlights the errors that are produced by various models, while comparing modeling results with finite element and experimental data.

## 2. Lumped-parameter modeling

A paddle micro cantilever is sketched in Fig. 1 (a) whose out-of-plane bending is monitored. Lumped-parameter modeling enables analyzing this structure as a single degree-of-freedom member made up of a mass and a spring that are located at the free end of the cantilever, as indicated in Fig. 1 (b).

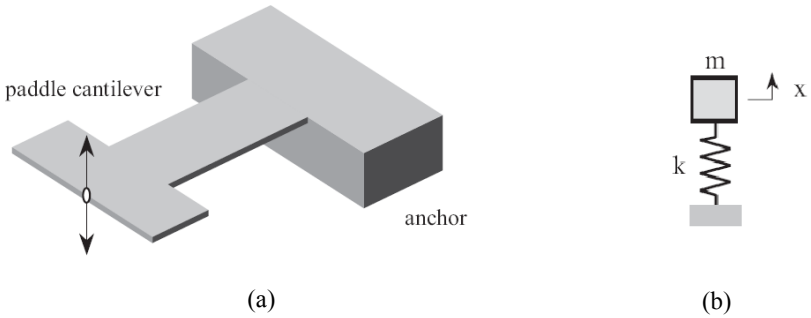


Figure 1. Paddle micro cantilever in out-of-plane bending motion: (a) three-dimensional sketch; (b) equivalent lumped-parameter model

Figure 2 shows three different lumped-parameter models that can describe the out-of-plane bending resonant response of the paddle cantilever of Fig. 1 (member # 1 is the tip paddle segment whereas member # 2 is the root segment of Fig. 1).

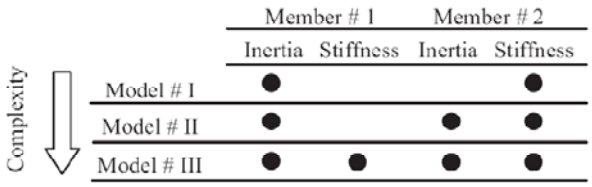


Figure 2. Modeling variants of a paddle cantilever

Model # 1, the simplest one, only takes into consideration the inertia of the free tip segment and the compliance (stiffness) of the root part. A more refined model can be developed which considers that inertia results from both segments whereas stiffness is attributed only to the root segment, similarly to the first model. Finally, a more complete lumped-parameter model which includes inertia and stiffness contributions from both segments

is model #3. Figure 3 plots the ratio of the Model # I natural frequency to the Model # II natural frequency, whereas Fig. 4 plots the ratio of the Model # I natural frequency to the Model # III natural frequency

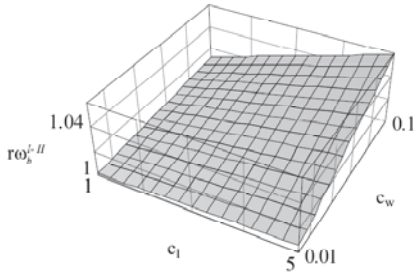


Figure 3. Comparison between Model # 1 and Model # 2 out-of-plane natural frequencies

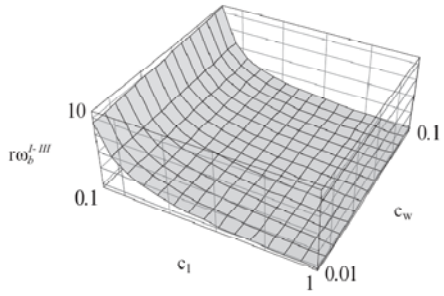


Figure 4. Comparison between Model # 1 and Model # 3 out-of-plane natural frequencies

## References

[1] Ilic B, Craighead HG, Krylov S, Senaratne W, Ober C, Neuzil P. Attogram detection using nanoelectromechanical oscillators. *Journal of Applied Physics*; 2004; **95 (7)**: 3694-3701.

[2] Lobontiu N. *Mechanical Microresonators: Modeling, Design, and Applications*, McGraw-Hill, New York, 2005.

[3] Lobontiu N, Ilic B, Garcia E, Reissman T, Craighead HG. Modeling of nanofabricated paddle bridges for resonant mass sensing. *Review of Scientific Instruments*; 2006; 77: 073301-1 - 073301-9.

Proceedings of the 6th International Conference on
Computation of Shell and Spatial Structures
IASS-IACM 2008: "Spanning Nano to Mega"
28-31 May 2008, Cornell University, Ithaca, NY, USA
John F. ABEL and J. Robert COOKE (eds.)

# The response of a cantilever microbeam with a plate attached to its tip to mechanical shock

Hassen OUAKAD[*], Haider N. ARAFAT[§], and Mohammad I YOUNIS[*]

[*] Department of Mechanical Engineering, State University of New York at Binghamton, Binghamton, NY 13902, myounis@binghamton.edu (corresponding author).
[§] Dynamic Loads, Cessna Aircraft Company, Wichita, KS, 67215, hnarafat@cessna.textron.com.

## Abstract

We present an investigation into the response of a cantilever microbeam with a plate attached to its tip to mechanical shock. This structural configuration is found in numerous MEMS devices, such as gas sensors and capacitive accelerometers. To ensure reliable operation of these devices, their performance under mechanical shock has to be analyzed. In this work, a nonlinear Euler-Bernoulli beam model with a rigid plate attached to its tip is utilized. The model accounts for the geometric and inertia nonlinearities of the microbeam. The system of integro-partial-differential equations is discretized using a Galerkin procedure to extract a reduced-order model, which is then used for dynamic simulations of the system responses. The system is also modelled using the nonlinear finite element software ANSYS. The influences of the different components of nonlinearity are examined and the results of the nonlinear beam theory are compared with the results of a linear beam theory and the results of ANSYS. It is found that the effect of the plate is to enhance the dynamic, as opposed to the quasi-static, response of the microbeam to mechanical shock.

## 1. Introduction

Cantilever beams with an almost rigid plate at their free end (i.e.; a paddle) are common mechanical systems in MEMS and sensors applications [1]. In mass and gas sensors applications, the plate provides a big surface area that can be coated with materials that enhances sensitivity [2]. In accelerometers and inertia sensors, the plate provides adequate inertia which amplifies the beam response and thereby, also increasing sensitivity. However, with the attractive advantages of cantilever-plate microbeams comes the disadvantage of the system being more vulnerable to stiction and collapse failures due to shock and impact. The big mass at the microbeam tip means higher motion sensitivity to dynamic disturbances. Therefore, under dynamic shock loading, the microbeams can deflect significantly. These large deflections can cause hard contact with surrounding stationary components on the MEMS chip, which may break the microbeam or cause other damage. In applications such as capacitive sensors, this large deflection can result in a contact with the substrate, which may lead to short circuit and stiction problems [3]. Microstructures, including cantilever microbeams, can be exposed to shock during fabrication, shipping, storage, and end-use, such as in space applications and harsh environments in military applications. When implemented in portable devices and electronics, such as cell phones, these microbeams have to survive drop testing on hard surfaces, which is crucial for the commercialization of MEMS.

Many microstructures experience mechanical shock as quasi-static loads. This is because these systems have high natural frequencies and hence, their natural periods are much smaller than the typical duration of shock loads [4]. Cantilever microbeams however are characterized by having low stiffness compared to other microbeams and micro-structures with other boundary conditions. Hence, their natural frequencies are relatively low and this means that they can experience mechanical shock as a dynamic load. This possibility increases further when a proof mass or a paddle is attached at the beam's tip because the added mass further lowers the system natural frequencies. When subjected to mechanical shock, cantilever microbeams can deflect significantly before they hit the substrate or other stationary parts. Under large deflection, the use of a linear beam theory to simulate the response may be inaccurate or questionable. In this work, we investigate the

response of a cantilever microbeam-paddle system under mechanical shock using a reduced-order model ROM [5] based on a nonlinear Euler-Bernoulli beam model.

## 2. Problem Formulation

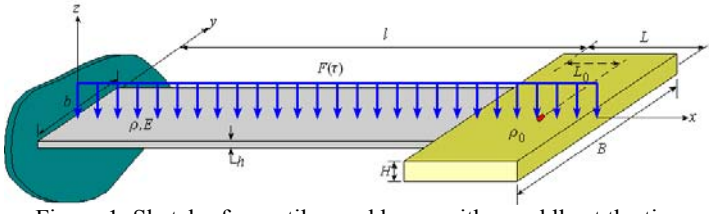


Figure 1: Sketch of a cantilevered beam with a paddle at the tip.

Figure 1 shows a schematic representation of the microbeam-plate (paddle) system. The microbeam has a mass per unit length $m$, material density $\rho$, modulus of elasticity $E$, length $l$, width $b$, and thickness $h$. The rigid plate has a mass $M_0$, length $L$, width $B$, and thickness $H$. The moment of inertia of the plate about its center of mass, located a distance $L_0$ from the end of the beam, is

$$J_0 = \tfrac{1}{12} M_0 \left(H^2 + L^2\right) \simeq \tfrac{1}{12} M_0 L^2 \quad \text{for} \quad H \ll L \tag{1}$$

Let $w(s,\tau)$ be the dimensional transverse deflection of the beam at a point $s$ along the elastic axis and dimensional time $\tau$. Neglecting the effects of the beam rotary inertia and the plate nonlinear inertia and following the nonlinear Euler-Bernoulli beam theory, the equation of can be written as [6]:

$$m\frac{\partial^2 w}{\partial \tau^2} + EI\frac{\partial^4 w}{\partial s^4} + C\frac{\partial w}{\partial \tau} = -EI\frac{\partial}{\partial s}\left[\frac{\partial w}{\partial s}\frac{\partial}{\partial s}\left(\frac{\partial w}{\partial s}\frac{\partial^2 w}{\partial s^2}\right)\right] - \frac{1}{2}m\frac{\partial}{\partial s}\left\{\frac{\partial w}{\partial s}\int_l^s\left[\frac{\partial^2}{\partial \tau^2}\int_0^s\left(\frac{\partial w}{\partial s}\right)^2 ds\right]ds\right\} + F(\tau) \tag{2}$$

where $C$ is the dimensional damping coefficient and $F(\tau)$ is a dimensional external excitation assumed to be uniformly distributed along the beam. The first two terms on the right-side of the equation are cubic nonlinearities that result from geometry (large-amplitude bending deflections) and inertia (longitudinal-bending deflections coupling) effects, respectively. The associated boundary conditions are

$$\begin{aligned} w(0,\tau) &= 0 \\ \frac{\partial w}{\partial s}(0,\tau) &= 0 \\ EI\frac{\partial^2 w}{\partial s^2}(l,\tau) + M_0 L_0\frac{\partial^2 w}{\partial \tau^2}(l,\tau) + \left(J_0 + M_0 L_0^2\right)\frac{\partial^3 w}{\partial s \partial \tau^2}(l,\tau) &= \frac{L^2}{2}F(\tau) \\ EI\frac{\partial^3 w}{\partial s^3}(l,\tau) - M_0\frac{\partial^2 w}{\partial \tau^2}(l,\tau) - M_0 L_0\frac{\partial^3 w}{\partial s \partial \tau^2}(l,\tau) &= -LF(\tau) \end{aligned} \tag{3}$$

Equations (2)-(3) are discretized using a Galerkin procedure to yield a reduced-order model (ROM) [5]. The ROM consists of a set of nonlinear ordinary-differential equations in terms of modal coordinates that is integrated numerically with time to simulate the dynamic response.

## 2. Results

As a case study, we investigate the response of a microbeam-paddle system implemented in a biomolecular sensor [2]. The geometric and physical characteristics of the system, shown in Figure 1, are given in Table 1. We first examine the convergence of the ROM as the number of modes is increased. Figure 2 shows the response of the system obtained by simulating the ROM for different numbers of the first three modes and for two shock durations, which span the expected duration during a drop-table test. It follows from Figure 2 that the use of two modes predicts accurately the response of the system. Next, we verify the simulation results by comparing them with results generated by modeling the system with a nonlinear finite-element model of the software ANSYS [7]. Figure 3(a) shows comparisons between the results of the ROM employing the first two modes (solid line) and the FE model results (dots) for a shock duration of $0.2ms$. Figure 3(b) shows the ANSYS

FE model. We note from Figure 3(a) full agreement between the two-mode nonlinear beam model and the FE model, which shows that the microbeam response changes nonlinearly with the shock amplitude. We also conclude from this figure that the ROM is capable of capturing the dynamic behavior of a nonlinearly behaving microstructure using a few numbers of modes, which is computationally cheap compared to using a nonlinear FE model for transient simulations.

Table 1: Geometric and physical parameters of the microbeam-plate system [2].

| $l$ | $b$ | $h$ | $d$ | $E$ | $\rho$ | $L$ | $B$ | $H$ | $\rho_0$ |
|---|---|---|---|---|---|---|---|---|---|
| 200 $\mu m$ | 40 $\mu m$ | 0.5 $\mu m$ | 4 $\mu m$ | 85 $GPa$ | 3000 $Kg/m^3$ | 100 $\mu m$ | 100 $\mu m$ | 0.5 $\mu m$ | 3000 $Kg/m^3$ |

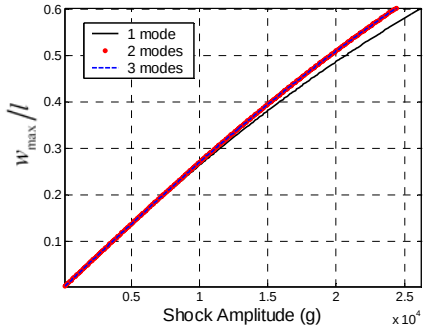


(a) $T_s$ =0.2 *ms*.

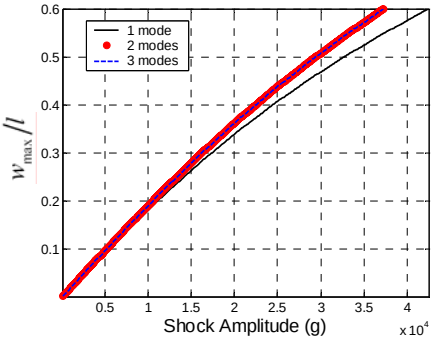


(b) $T_s$ = 1 *ms*.

Figure 2: The response of the fully nonlinear undamped cantilever microbeam-plate system using a reduced-order model with different numbers of modes and for two shock durations $T_s$.

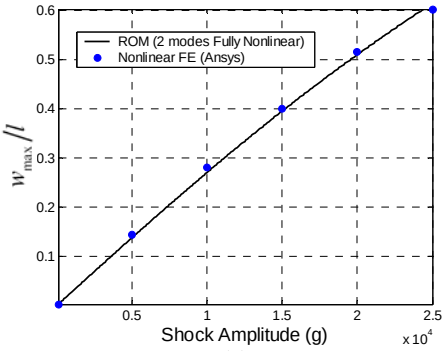


**(a)**

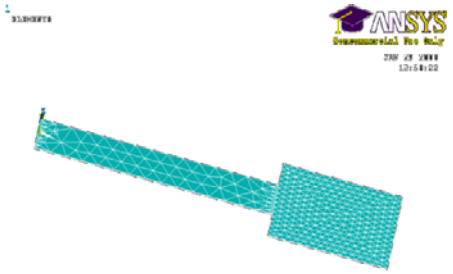


(b)

Figure 3: (a) The response of the cantilever microbeam-plate system using the reduced-order model (solid line) and the nonlinear FE model (dots) for a shock duration $T_s$ =0.2 *ms* and (b) the FE model in ANSYS [7].

The difference in the results between linear and nonlinear models is illustrated in Figure 4. The figure shows comparisons of the system response to shock using four different beam models: linear, fully nonlinear, geometric nonlinear only, and inertia nonlinear only. It is noted from this figure that the dominant nonlinearity of the system is mainly geometric. The influence of varying the mass ratio $M \equiv M_0 / ml$ of the plate to the beam on the system response is illustrated in Figure 5 for three cases: $M$ = 0 (no plate), $M$ = 1.25 (the system defined in Table 1), and $M$ = 2. The natural periods of the system are calculated to be 0.91 *ms,* 0.41 *ms,* and 0.311 *ms,* respectively. It is evident that as $M$ varies, it significantly influences the natural period of the system. In turn, this affects the nature of the response, whether it is quasi-static or dynamic. Figure 5 also shows that the

addition of the plate to the microbeam tip makes the system more likely to hit the substrate under a shock load since the tip deflection is larger.

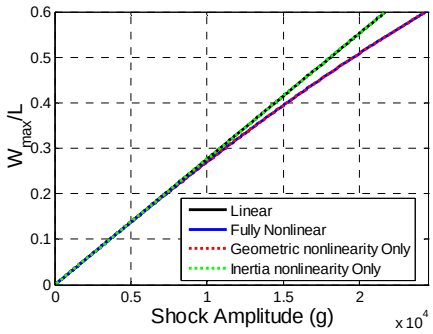


(a) $T_s = 0.2$ *ms*.

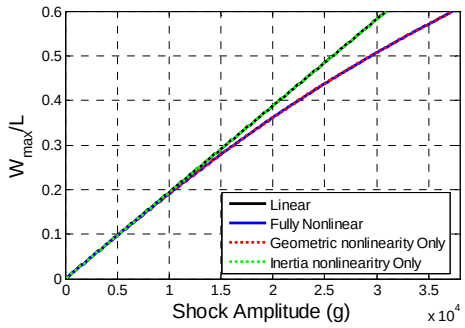


(b) $T_s = 1$ *ms*.

Figure 4: Comparison of the undamped response of the cantilever microbeam-plate system generated using a linear beam model (solid black), a fully nonlinear beam model (solid blue), a geometric-only nonlinear beam model (dashed red) and an inertia-only nonlinear beam model (dashed green).

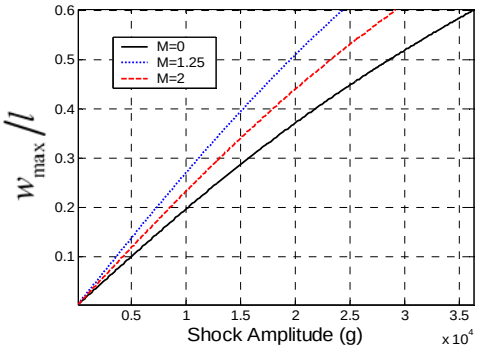


Figure 5: Comparison of the undamped response of the cantilever microbeam-plate system when varying the mass ratio $M$ for a shock duration $T_s = 0.2$ *ms*.

## References

[1] Krylov S, and Maimon R, Pull-in dynamics of an elastic beam actuated by continuously distributed electrostatic force, *Transactions of the ASME*: 2004; 332-342.

[2] Min Yue, Henry Lin, Daniel E. Dedrick, Srinath Satyanarayana, Arunava Majumdar, Aditya S. Bedekar, Jerry W. Jenkins, and Shivshankar Sundaram, A 2-D microcantilever array for multiplexed biomolecular analysis, *Journal Of Microelectromechanical Systems*: 2004; 290-299

[3] Younis MI, Miles R, and Jordy D, Investigation of the response of microstructures under the combined effect of mechanical shock and electrostatic forces, *Journal of Micromechanics and Microengineering*: 2006; 2463-2474.

[4] Younis MI, Jordy D, and Pitarresi J, Computationally efficient approaches to characterize the dynamic response of microstructures under mechanical shock, *Journal of Microelectromechanical Systems*: 2007; 628-638.

[5] Younis MI, Abdel-Rahman EM, and Nayfeh AH, A reduced-order model for electrically actuated microbeam-based MEMS, *Journal of Microelectromechanical Systems*: 2003; 672-680.

[6] Arafat HN, *Nonlinear response of cantilever beams*, Ph.D. Dissertation: 1999; Virginia Tech, Blacksburg.

[7] ANSYS, Inc. 2007 Version 11, www.ANSYS.com; 2008.

Proceedings of the 6th International Conference on
Computation of Shell and Spatial Structures
IASS-IACM 2008: "Spanning Nano to Mega"
28-31 May 2008, Cornell University, Ithaca, NY, USA
John F. ABEL and J. Robert COOKE (eds.)

# Switch triggered by mass threshold

Mohammad I YOUNIS * and Fadi M. AL SALEEM

* Department of Mechanical Engineering, State University of New York at Binghamton
Binghamton, NY 13902, myounis@binghamton.edu

## Abstract

This study presents an effort to explore the exploitation of the dynamic pull-in and the escape-from-a-potential-well phenomena in MEMS to realize novel mass detectors of desirable characteristics and functionalities. These instabilities are induced by exciting a microstructure with a nonlinear forcing composed of a DC parallel-plate electrostatic load and an AC harmonic load. The frequency of the AC load is tuned to be near the fundamental natural frequency of the structure (primary-resonance) or its multiples (sub-harmonic-resonance). In this work, we discuss the concept of a switch triggered by mass threshold (STMT). This device has the potential of serving as a smart switch that combines the functions of two devices: a sensitive gas/mass sensor and an electro-mechanical switch. The switch can send a strong electrical signal as a sign of mass detection, which can be used to actuate an alarming system or to activate a defensive or a security system. As case studies, this device concept is demonstrated by simulations on clamped-clamped microbeams. Results are presented using long-time integration for the equations of motion of a reduced-order model. Then, experimental data are presented on a mille-micro scale capacitive sensor demonstrating the idea of the STMT.

## 1. Switches based on clamped-clamped beams

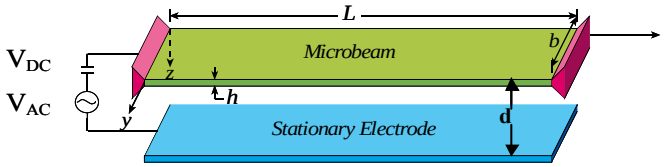


**Figure 1.** A MEMS parallel-plate capacitor showing a dynamic AC+DC actuation.

There has been extensive research in recent years in the field of mass sensing and detection [1]. This is driven primarily by the increasing demand to push the limits of mass sensing to enable reliable and precise detection of extremely small masses, such as those of viruses and DNA molecules. Also, this has been boosted by the need to detect very low gas concentration for gas sensing applications. In addition, lowering the cost of mass sensors and achieving smart and multi-functionality on a single chip have been major driving forces. This study presents an attempt to explore alternative methods to achieve some of these goals by utilizing the complexity in the dynamics of electrostatically-actuated Micro-electro-mechanical systems (MEMS).

The focus of this work is on resonant microsensors employing microbeams. These microbeams are excited by a DC load superimposed to an AC harmonic load, Figure 1. Next, we show simulation results of a clamped-clamped microbeam using time integration of a microbeam-reduced-order model [2]. The studied microbeam has length $L$=510 $\mu m$, thickness $h$=1.5 $\mu m$, width $b$=100 $\mu m$, and a gap width separating the microbeam from the substrate $d$=1.18 $\mu m$. The microbeam is biased by $V_{AC}$ =2 V and placed in a reduced pressure with quality factor equal 1000. The pull-in voltage for the microbeam due to DC voltage only is $V_{DC}$ =4.8 V. The natural frequency of the microbeam is $\omega_{natural}$ = 23.9 $\omega_{Universal}$, where $\omega_{Universal}$ is a universal characteristic frequency for a microbeam of any boundary conditions. It is expressed as $\omega_{Universal} = \sqrt{Ebh^3/12mL^3}$, where $m$ is the mass of the beam. Figure 2a shows that by increasing the AC load from $V_{AC}$=0.01 V to $V_{AC}$=0.1 V, the frequency response curve is terminated by dynamic pull-in, which is remarked by a slope of the frequency

response curve approaching infinity [3,4]. As $V_{AC}$ is increased more, a band of frequencies is born, in which the microbeam cannot have a state of steady-state oscillation, such as the case of $V_{AC}$=0.5 V. In another words, the microbeam tends to escape from the potential well of the electrostatic force to dynamic pull-in [3-5]. The escape phenomenon is further illustrated in Figure 2b.

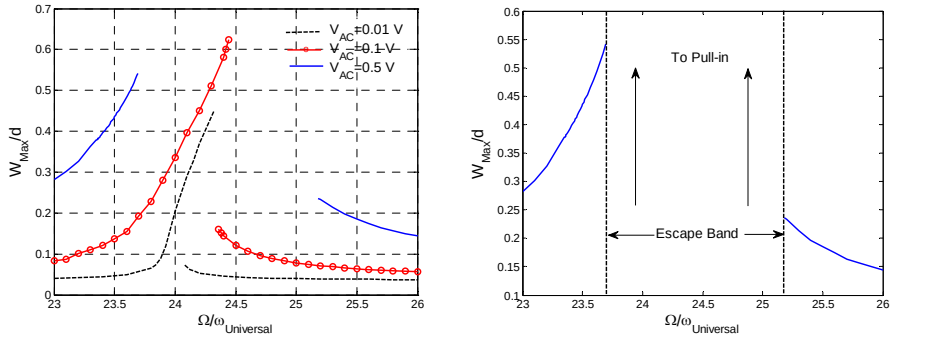


**Figure 2.** Frequency-response curves of a clamped-clamped microbeam excited near its first natural frequency for various values of AC loads. Figure b is for the case of $V_{AC}$=0.5 V showing the escape-to-pull-in frequency band.

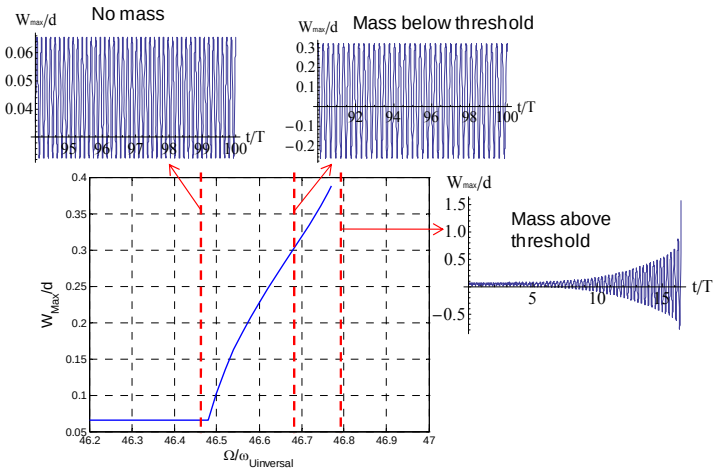


**Figure 3.** Frequency-response curve and time histories of a clamped-clamped microbeam excited at sub harmonic resonance illustrating its utilization for STMT and MSAR at the same time. The first dashed line to the left indicates the original operating point and the other dashed lines indicate the new operating points upon the detection of various amount of mass.

Figure 2b shows that by tuning some parameters of the system, $V_{AC}$, $V_{DC}$, and damping, a frequency band is generated where an oscillator cannot have a stable state (escape phenomenon). This means that if a microbeam is excited by an AC load of a frequency in the escape band, it must go directly to pull-in. We propose to utilize this phenomenon to design a smart Switch Triggered by Mass Threshold STMT. In this concept, a microbeam, which is coated with a material sensitive to a specific analyte, is excited by a combination of a DC and AC harmonic load of a fixed frequency $\Omega$ below the escape band of frequencies, for example at $\Omega/\omega_{Universal}$=23.5 in Figure 2b. When the microbeam detects the existence of the specific substance desired to be detected, its mass *m* increases, $\omega_{Universal}=\sqrt{Ebh^3/12mL^3}$ decreases, and hence the ratio $\Omega/\omega_{Universal}$ increases and shifts to the right. The shift can be calibrated such the new $\Omega/\omega_{Universal}$ lies in the escape band of frequencies when detecting a certain amount of analyte above a specific mass threshold (this can be a concentration threshold for

gases). Hence, the microbeam collapses to close an electric circuit to indicate the presence of the gas and at the same time sends an electrical signal, which can be used for alarming or any other useful function.

Exciting the microbeam at twice its natural frequency (sub-harmonic resonance of order one half) leads to another interesting application combining a switch and a mass sensor. Figure 3 demonstrates this idea when exciting the microbeam for $V_{DC}$ =2, $V_{AC}$ =0.6 V and a quality factor equal 100. To realize a mass sensor, the microbeam needs to operate at the flat regime of the frequency-response curve, as shown in Figure 3, for instance at $\Omega/\omega_{Universal}$=46.45 with $W_{max}/d$=0.06. If the microbeam picks or absorbs an analyte, the operating point of the microbeam will shift to the right to ride the sub-harmonic resonance curve, for example at $\Omega/\omega_{Universal}$=46.69 with $W_{max}/d$=0.3. This new amplified response of the microbeam can be related to the amount of mass absorbed or detected, thereby realizing a mass sensor. If the amount of detected mass exceeds a specific threshold, $\Omega/\omega_{Universal}$ shift to the escape band of frequencies, for example $\Omega/\omega_{Universal}$=46.8, forcing the microbeam to collapse as a switch (STMT).

## 2. Switched based on cantilever beams

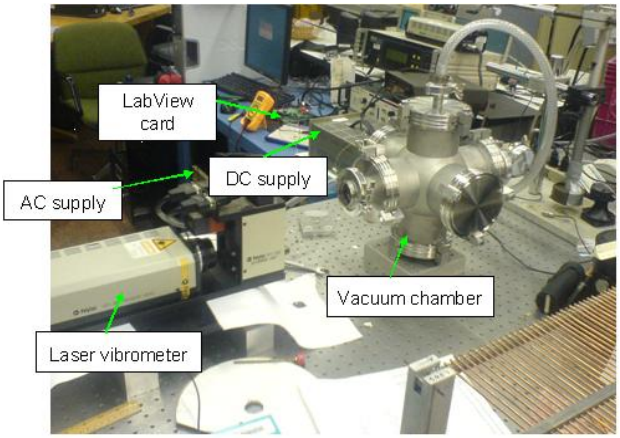


**Figure 4:** The experimental setup used for testing the capacitive accelerometers under vacuum.

A capacitive accelerometer sensor, fabricated by Sensata Technologies [5], was used for an experimental study to demonstrate the idea of the STMT. The sensor is made up of an alloy 42 cantilever beam of thickness *150* μm with a proof mass attached to its tip. Cantilever microbeams do not suffer mid-plane stretching, which is cubic nonlinearity, as the case of clamped-clamped microbeams. Hence, in the presence of nonlinear electrostatic forces, which are quadratic in nature, they exhibit pure softening behavior at large deflection. The sensor was placed in vacuum chamber with a quartz window at a pressure less than 2.0 torr (Figure 4). A tiny amount of glue was added to the capacitive accelerometer surface, Figure 5. We found that the added mass cause a shift in the fundamental natural frequency of the mass sensor by *3.0* Hz.

Next, we drive the sensor around its primary resonance with high values of AC and DC load. Figure 6a shows the device frequency response before and after adding the same mass of Figure 5. A frequency shift of *3 Hz* is observed due to the added mass. If we consider, for example, the excitation frequency of *170* Hz for the no added mass case in Figure 6a we notice that the sensor response is stable. On the other hand, at the same excitation frequency when the mass is added the sensor response becomes unstable and eventually goes to pull-in. Next, we excite the cantilever at twice its natural frequency. Figure 6b shows sub-harmonic resonance before and after adding the same masses of Figure 5. It is clear from the figure that in both plots the frequency shift as a result of the added mass is doubled compared to the primary resonance. This in itself can be utilized

to amplify the sensitivity of resonant mass sensors. The same idea for the switch applies for sub-harmonic resonance. For example if we excite the microbeam in the shaded area in Figure 6b the device response is stable before mass detection. On the other hand, when the mass is added, the sensor response is unstable and eventually goes to pull-in as a switch. One can note that the transition from low-amplitude stable oscillation to unstable response (pull-in) in this case is much dramatic compared to the primary-resonance case.

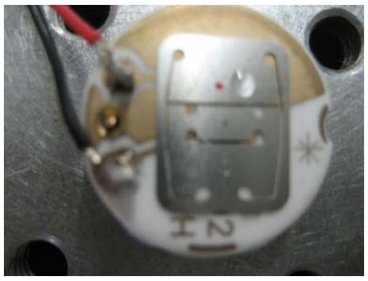

**Figure 5:** The capacitive accelerometer showing the added mass.

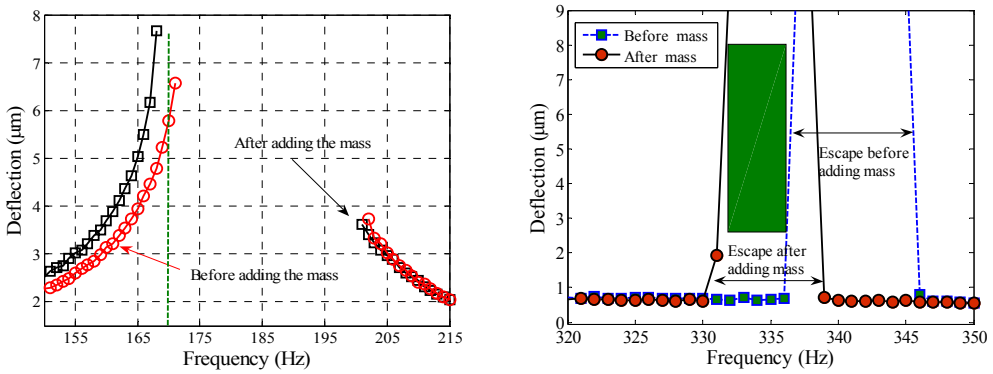


**Figure 6:** (a): Primary-resonance escape zone before and after adding a mass causing a frequency shift of *3.0* Hz *(Vdc=80* Volt and *Vac=36.9* Volt). (b): Sub-harmonic-resonance escape zone before and after adding masses (*Vdc=95* Volt and *Vac=37.2* Volt*).*

## References

[1] Lange, D., Brand, O., and Baltes, H., "CMOS cantilever sensor systems: atomic-force microscopy and gas sensing applications," Springer, Berlin, (2002).

[2] Younis, M. I., Abdel-Rahman, E. M., and Nayfeh, A. H., "A reduced-order model for electrically actuated microbeam-based MEMS," J. Microelectromech. Syst., Vol. 12, pp. 672--680, 2003.

[3] Nayfeh, A. H., Younis, M. I., and Abdel-Rahman, E. M., "Dynamic pull-in phenomenon in MEMS resonators," Nonl. Dyn., Vol. 48, pp. 153-163, (2007).

[4] Nayfeh, A. H., and Younis, M. I., "Dynamics of MEMS resonators under superharmonic and subharmonic excitations," J. Micromech. Microeng., Vol. 15, pp. 1840-1847, (2005).

[5] Thompson, J. M. T., and Stewart, H. B., "Nonlinear dynamics and chaos," Wiley, New York, (2001).

[6] www.sensata.com

Proceedings of the 6th International Conference on
Computation of Shell and Spatial Structures
IASS-IACM 2008: "Spanning Nano to Mega"
28-31 May 2008, Cornell University, Ithaca, NY, USA
John F. ABEL and J. Robert COOKE (eds.)

# Adhesion of freestanding beams and its application to micro- and nano-structures

Kai-tak WAN *

* Mechanical and Industrial Engineering, Northeastern University
Rm 334 Snell Engineering Center, 340 Huntington Ave, Boston, MA 02115
ktwan@coe.neu.edu

## Abstract

A rectangular beam is clamped at both ends. A rectangular planar punch adhered to the beam is pulled away to shrink the contact area. When the contact reduces to a line, the beam detaches spontaneously, and the phenomenon is known as "pinch-off". The delamination trajectory in the presence of tensile residual stress is established based on a thermodynamic energy balance. The model is applied to (i) optimization of a micro-electromechanical-systems radio frequency switch (MEMS-RF-switch), (ii) criterion for instability of micro-network of trusses, and (iii) topographical measurement of flexible structures using atomic force microscope (AFM).

## 1. Introduction

Adhesion between micro- and nano- scale surfaces leads to significant impacts on many devices behavior. An obvious example is the undesirable stiction in many moveable parts in micro-electromechanical systems (MEMS), leading to operation failure, reduction of reliability and life span. A typical MEMS-RF switch is chosen here to demonstrate the mechanical consequences due to adhesion. Rather than tackling the full fledged coupled electro-mechanical behavior, we will construct a simple mechanical model to derive the adhesion-delamination mechanics that is based on linear elasticity, intersurface forces, thermodynamic energy balance without loss of generality.

The model is further extended to account for the stability of micro-beam networks. In the presence of high relative humidity, van der Waals interactions, and stray electrostatic charges, adhesion might cause the structure to collapse, depending on the strength of surface forces, the mechanical properties of the materials, and the geometrical arrangement. We attempt to derive the critical conditions for an inevitable instability. Another application is to gauge the viability of topographical and adhesion measurements of flexible structures or membranes using an AFM or nano-indentation.

## 2. Theory

Figure 1 shows a beam with unit width, length, $2l$, and thickness, $h$, bending rigidity, $\kappa = Eh^3 / 12\,(1-\nu^2)$, elastic modulus, $E$, Poisson's ratio, $\nu$, and tensile residual stress, $\sigma_0$, being clamped at both ends. A rigid punch spanning the beam width and length $2l$ makes an intimate contact with the suspended bridge, with an interfacial adhesion energy, $\gamma$. An external tensile force, $F$, applied to the punch deforms the beam to a profile, $w(x)$, and causes the beam to delamination from the punch and the contact length to shrink to $c$ ($< l$). Once the punch displacement, $w_0$, reaches a critical threshold, the contact reduces to a line and the beam spontaneously detaches from the punch surface, a phenomenon known as "pinch-off". Linear elasticity requires the beam profile to be governed by [1]

$$\underbrace{\kappa.\nabla^4 w}_{\text{Plate}-\text{bending}} - \underbrace{\sigma_0 h.\nabla^2 w}_{\text{Tensile Residual Stress}} = \underbrace{F.\delta(x)}_{\text{External Load}} \qquad (1)$$

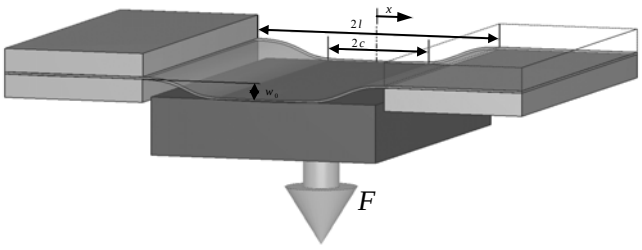


Fig.1. A clamped beam (or membrane) delaminating from a rigid punch surface.

where $\delta(x)$ is the delta function. The normalized variables, $\omega = w / h$, $\xi = x / l$, $\lambda = c / l$, $\varphi = (l^3/2\kappa h)F$, $\beta = (l/\kappa^{1/2})\sigma_0^{1/2}$ and $\Gamma = (l^4/\kappa h^2)\,\gamma$, are adopted hereafter. Solving (1) with proper boundary conditions,

$$\omega_0 = \omega(\xi = \lambda) = \varphi \left\{ -\frac{2}{\beta^3}\tanh\left[\frac{\beta(1-\lambda)}{2}\right] + \frac{1}{\beta^2}(1-\lambda) \right\} \tag{2}$$

The total energy of the system is given by $U_T = (1/2)\,F.w_0 - \gamma\,.\,c$, where the first term denotes the elastic energy stored in the beam and the second term the energy required to create new surfaces. Thermodynamic equilibrium occurs when $\partial U_T / \partial c = 0$,

$$\Gamma = \varphi^2 \left\{ \frac{1}{2\beta^2}\tanh^2\left[\frac{\beta(1-\lambda)}{2}\right] \right\} \tag{3}$$

The relationship between the measureable quantities, $F$, $w_0$ and $c$ can be found by simultaneously solving (2) and (3). The constitutive relation is conveniently cast in the form of $F \propto (w_0)^n$ with

$$n = \frac{\partial(\log F)}{\partial(\log w_0)} = \frac{2\tanh[\beta(1-\lambda)/2] - \beta(1-\lambda)}{\sinh[\beta(1-\lambda)/2] - \beta(1-\lambda)} \tag{4}$$

The delamination trajectory is illustrated in Figures 2 and 3. At small punch displacement, the beam deformation is mainly governed by plate-bending, while large displacement leads to membrane stretching.

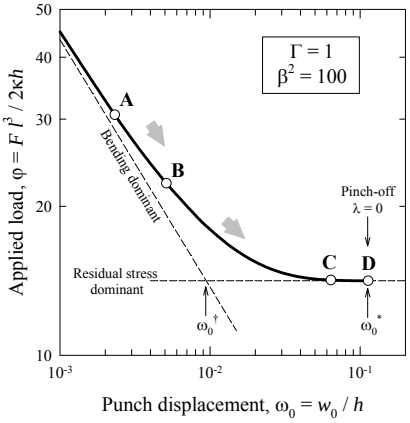


Fig.2. Delamination follows ABCD. Pinch-off occurs at D. Plate-bending to membrane-stretching transition occurs at $\omega_0^{\dagger}$.

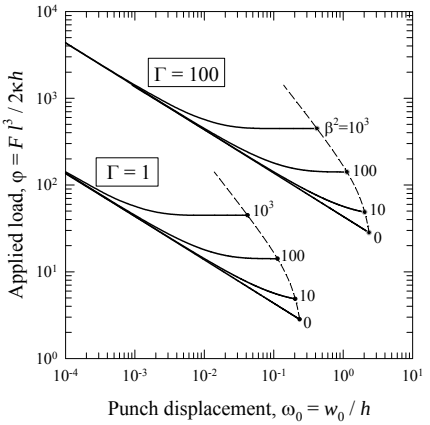


Fig.3. Delamination trajectories for ranges of adhesion and residual stress. Pinch-off occurs at the terminal points of each curve.

## 3. Applications

The above model is applicable to a number of micro- and nano-structures.

### 3.1 Microelectromechanical systems (MEMS)

Figure 4 shows a typical MEMS-RF-switch with a suspended bridge over an electrostatic pad. In the presence of an applied potential applied to the pad, the moveable beam is compelled to make an intimate contact with the pad giving rise to an electrical signal. Removal of the applied voltage causes the bridge to recover its non-deformed geometry and a reverse of signal. The presence of adhesion at the film-substrate interface, however, obstructs the elastic recovery. Our new model resembles this geometry (c.f. Fig.1), though the electrostatic attraction is yet to be considered [2]. In fact, the adhesion-delamination mechanics enhances better design and optimizes performance, especially when both adhesion and residual stress are coupled as a result of environment, thermal mismatch and heating due to operation.

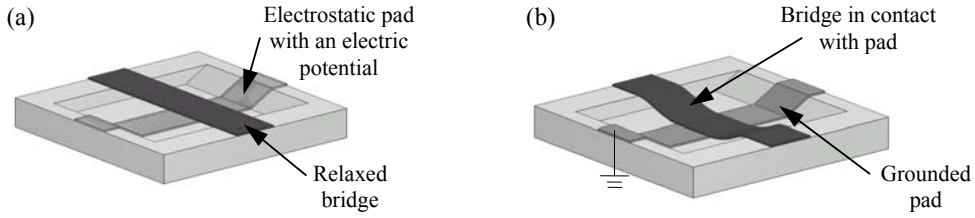


Fig.4. Sketch of a MEMS-RF-switch: (a) OFF and (b) ON signals.

### 3.2 Micro-beams network

Wu et al [3] constructed micro-beam networks free of residual stress. In the presence of strong intersurface forces, instability sets in and the structure collapses. Fig.5. shows two adjacent beams adhering to each other. Our new model predicts the critical conditions. If the beams are deformed by pure bending, the maximum allowable beam length is given by

$$l_d = C \left\{ \frac{Eh^3}{\gamma} \right\}^{1/4} (w_0^*)^{1/2} \tag{5}$$

where $2w_0^*$ is the inter-beam separation. and $C = (48)^{1/4} \approx 2.632$. If membrane-stretching replaces plate-bending as the dominant deformation mode, the critical condition is modified to

$$l_d = 2\left\{ \frac{Eh}{\gamma} \right\}^{1/2} w_0^* \tag{6}$$

To design a stable network structure, either the beam span is shorter than $l_d$ or the separation is larger than the critical value of $w_0^*$. Simple modifications can be made to accommodate beams with circular cross-section.

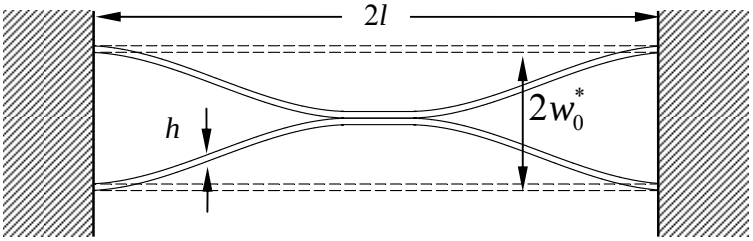


Fig.5. Adhesion of two adjacent beams.

### 3.3 Micro-beams network

The new model is applicable in mechanical characterization of pre-stressed nano-wires and nano-springs. When a central load is applied to the mid-span of the specimen via an atomic force microscope (AFM), the distance traveled by the AFM tip can be measured to yield the materials parameters and the residual stress using (2) to (4). The present work provides a rigorous analytical model for the coupling of bending moments and residual stress. Should the residual stress becomes compressive, all β's in the above equations are to be replaced by $i\,||\beta||$ with $i = \sqrt{(-1)}$.

## 4. Conclusion

An elastic model is built for the adhesion-delamination mechanics of a pre-stressed beam adhered to a rigid substrate. The model provides the performance equation relating (i) the structural index of mixed plate-bending and membrane-stretching, (ii) the measurable applied load, punch displacement (or the equivalent bridge-pad gap) and contact area, (iii) the geometrical factor of beam thickness and span, and (iv) the materials parameters of elastic modulus and Poisson ratio, adhesion energy at the film-substrate interface, and residual membrane stress. Specific applications in MEMS-RF switches and micro-beam network are discussed.

## Acknowledgement

Funding for this work by National Science Foundation CMS # 0757140 is acknowledged.

## References

[1] Wong MF, Duan G and Wan KT. Adhesion-delamination mechanics of a prestressed rectangular film adhered onto a rigid substrate. *Journal of Applied Physics* 2007; 101: 024903.

[2] Duan G and Wan KT. Analysis of one-dimensional and two-dimensional thin film "pull-in" phenomena under the influence of an electrostatic potential. *Journal of Applied Mechanics* 2007; 74: 927-934.

[3] Wu D, Fang N, Sun C and Zhang X. Stiction problems in releasing of 3D microstructures and its solution. *Sensors and Actuators A: Physical* 2006; 128: 109-115.

Proceedings of the 6th International Conference on
Computation of Shell and Spatial Structures
IASS-IACM 2008: Spanning Nano to Mega
28-31 May 2008, Cornell University, Ithaca, NY, USA
John F. ABEL and J. Robert COOKE (eds.)

# Modeling and dynamics of coupled dome-shaped micromechanical oscillators

Tuhin SAHAI and Alan T. ZEHNDER*

* Department of Theoretical and Applied Mechanics, 212 Kimball Hall, Cornell University, Ithaca, NY 14853, USA

## Abstract

Coupled micromechanical oscillators vibrating in synchrony have the potential for novel applications such as filters, neurocomputers and generators of clock signals in computer processors. In this work we analyze a feasible approach for constructing coupled micromechanical oscillators that synchronize. For this purpose we consider dome shaped micro-oscillators. These oscillators are fabricated by buckling a thin circular film of polysilicon, giving rise to a dome-shaped structure. They are thermally excited using resistive heating. The motion of the device is fed back into the heater using displacement measurement (e.g. capacitive pickup), driving the dome into stable limit cycle oscillations. Here we study the dynamics of one oscillator, and the ability of two micromechanical oscillators with different frequencies to synchronize via mechanical and electro-thermal coupling.

## 1 Introduction

Potential applications for synchronized micromechanical oscillators include signal processing [1], neurocomputing [2] and clock signal distribution for synchronous processors. In this work we develop a theoretical basis for the design of synchronized micro-oscillators. As an example, we analyze thermally excited dome shaped micro-oscillators, fabricated by buckling a thin, circular film of polysilicon [1]. The thin film of polysilicon is first deposited onto a layer of silicon dioxide. The deposition parameters are selected to ensure that the polysilicon is under large compressive (approximately $220$ MPa) stress. A circular region of silicon dioxide is etched away leaving a thin polysilicon disk under compression. This disk buckles to form a shallow dome. Typical oscillator diameters range from $10$ to $40$ $\mu$m. For our analysis we use a dome with outer diameter $40\mu$m, inner diameter of $4\mu$m, thickness $200$nm and a measured buckled height of $1\mu$m [1] (see Figure 1). We note that there is nothing special about this size and that our analysis can be repeated for domes of different dimensions.

In [1] the domes are driven using resistive heating and the motion optically detected [3]. Laser detection of motion may not be feasible for commercial applications, thus, we propose to detect motion using capacitive sensors or strain gauges, fabricated onto the surface of the oscillator. We propose a system in which the output of the displacement sensor is fed back into the resistive heater (Figure 2). This two way coupling of the motion to the thermal dynamics of the oscillator gives rise to limit cycle oscillations as seen in [1]. Before we study the dynamics of coupled oscillators, we need to construct a model for the dynamics of a single oscillator.

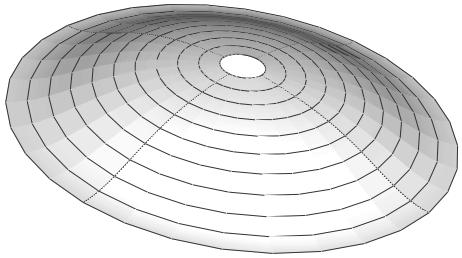

Figure 1: 3D view of the dome obtained from FEM simulations.

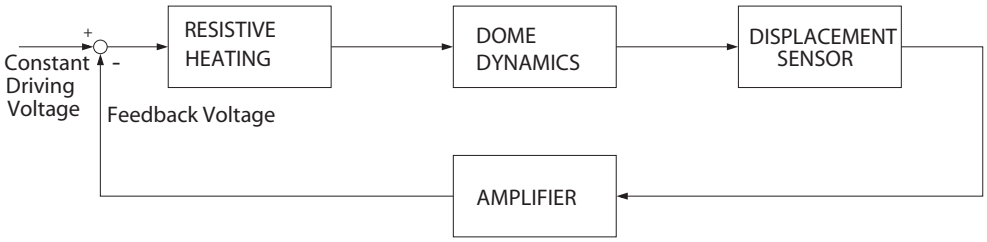


Figure 2: Block diagram of the proposed scheme to construct thermally driven micromechanical oscillators

# 2 Single Oscillator Model

## 2.1 Mechanical

To understand the dynamics and mechanical response of a single oscillator, we build an ordinary differential equation (ODE) model for oscillations of the dome about the buckled state. The post buckled shape of the dome is shown in Figure 1. We approximate the shape as

$$w(r) = \frac{1 - \cos(\frac{\pi(r-R)}{R})}{2}, \tag{1}$$

where $r$ is the radial distance from the center of the dome and $R$ is the outer radius of the dome oscillator, see figure 3. We use the axisymmetric von Kármán equations [4] to describe the nonlinear motion of a plate under compression. The outer boundary of the dome $R = 20\mu$m is considered to be clamped and the inner boundary $r_0 = 2\mu$m is free.

We constrain the dynamics of the plate to the mode shape given by Equation 1, by performing a Galerkin projection [4]. The result is a set of nonlinear ODEs that govern the dynamics of the dome oscillator. This ODE is of the form

$$m\ddot{A}(t) + \gamma'\dot{A}(t) + k_1 A(t) + k_3 A(t)^3 = 0, \tag{2}$$

where $m$ is the effective mass of the structure, $\gamma'$ is the damping, and $k_1$ and $k_3$ are the linear and and cubic stiffnesses calculated using the Galerkin projection procedure. The stiffness $k_1$ is found to be a linear function of $\sigma_R$, the radial

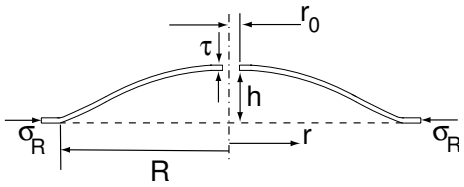


Figure 3: Dimensions of the dome oscillator (view of a radial section)

Table 1: Material Properties of Polysilicon

| | |
|---|---|
| $E$ | 160 GPa |
| $\rho$ | $2330\ \frac{kg}{m^3}$ |
| $\alpha$ | $2.6 \times 10^{-6}/K$ |
| $k$ | $20\ \frac{W}{mK}$ |
| $C_p$ | $753\ \frac{J}{kgK}$ |
| $\nu$ | 0.22 |

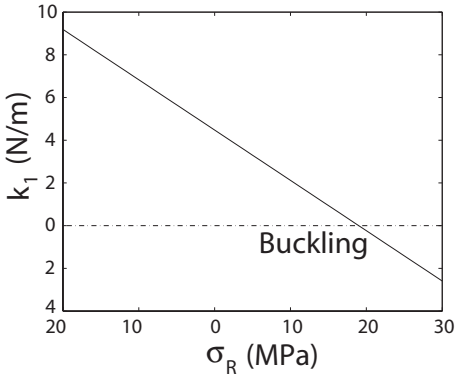


Figure 4: Variation of linear stiffness of plate with applied compressive stress at outer edge. Negative stiffness implies buckling.

stress at the outer edge of the disk, as plotted in Fig. 4. The cubic stiffness, however, is independent of $\sigma_R$. The value of $\sigma_R$ at which $k_1 = 0$ is the buckling load. For the dimensions and properties (from [6], [7] in Table 1) of our problem the critical buckling stress is found to be $\sigma_R \approx 19$ MPa. For $\sigma_R > 19$ MPa, $k_1 < 0$ and the structure assumes a buckled shape. The experimentally observed deflection of the dome is $\approx 1\mu m$ [3], which is found to correspond to $\sigma_R \approx 62$ MPa. Thus, the stress release due to buckling reduces the in-plane radial stress, $\sigma_R$, from 220 MPa to 62 MPa.

The resistive heater causes the dome to deflect upwards. This deflection has contributions from uniform heat expansion and higher compressive stresses at the boundary. We assume linearity and add the two effects. We find that the equilibrium of the structure varies linearly with temperature above ambient. Moving the origin to the buckled state, nondimensionalizing deflection by dividing by the thickness $\tau$ of the structure, and nondimensionalizing time gives

$$\ddot{z} + \frac{(\dot{z} - D\dot{T})}{Q} + h(T)(z - DT) + 3\sqrt{\frac{h(T)\beta}{2}}\tau(z - DT)^2 + \beta(z - DT)^3 = 0, \tag{3}$$

From thermal calculations we get $h(T) = 1 + 0.00023T$. Calculations on height increase give $D = \frac{D'}{\tau} \approx 6 \times 10^{-4}/K$. From the Galerkin projection we get $\beta \approx 0.5$. The quality factor, $Q$, of the device is found experimentally to be $\approx 2500$ [3].

## 2.2 Thermal

We build a thermal model of the structure by solving transient heat conduction on an annulus,

$$\frac{\partial T(r,t)}{\partial t} = \kappa \left[ \frac{\partial^2 T(r,t)}{\partial r^2} + \frac{1}{r}\frac{\partial T(r,t)}{\partial r} \right] + q, \tag{4}$$

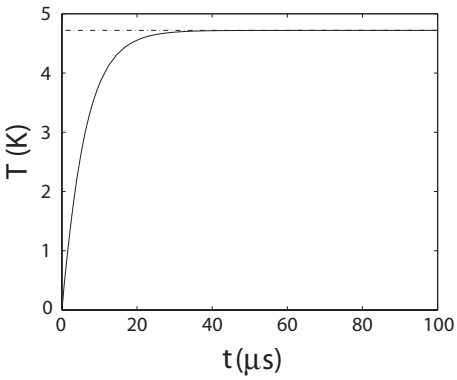


Figure 5: Variation of average temperature of annulus with time.

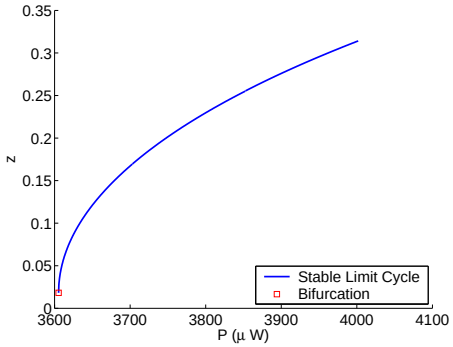


Figure 6: Maximum amplitude of oscillation of dome versus heat input, $z = \frac{w(r_0)}{\tau}$.

where $q$ is the heating due to the resistor. Heat loss due to radiation and convection are found to be negligible.

To solve equation 4, we break the solution into two parts: the steady state part and the transient part. The steady state part is the Poisson's equation on an annulus. After solving Poisson's equation, we solve for the transient part, which is the solution of the homogeneous heat equation with appropriate boundary conditions accounting for the steady state part. The solution for equation 4 is a function that depends on radial position and time. We now average this solution over the dome and model the response as a first order ODE,

$$\dot{T} = -B_T T + A_T P, \tag{5}$$

where $T$ is the temperature above ambient, $B_T$ is the rate of cooling due to conduction, $A_T$ is the inverse of the lumped thermal mass and $P$ is the input heat power. From figure 5, we find $A_T = 1.3 \times 10^{-3} \frac{K}{\mu W}$ and $B_T = 1.54 \times 10^{-1}$. Equations 3 and 5 give us a complete thermo-mechanical ODE model for dome dynamics.

# 3 Single Oscillator Dynamics

We model the dynamics of a single oscillator (equations 3 and 5). A close inspection of equation 3 shows that $z = DT$ is an equilibrium. Increasing the input power $P$ increases temperature which in turn deflects the structure. This equilibrium loses stability via a Hopf bifurcation [8] at $P = 2625\mu W$. The limit cycle (self oscillation) born at the Hopf bifurcation gains stability at a saddle-node bifurcation shown in figure 6.

# 4 Coupled Oscillators

We select the stable periodic motion at $P = 2585\mu W$ to study the response of two coupled oscillators. We detune one oscillator from the other by changing the frequency of the first by changing the $h(T)$ term. For the second oscillator the $h(T)$ term becomes $h_2(T) = \kappa + 0.00023T$, where $\kappa$ is a detuning parameter. We now study the ability of different forms of coupling to frequency lock the two oscillators.

## 4.1 Mechanical Coupling

In mechanical coupling we assume that the two detuned oscillators are coupled to each other by a spring. Physically this spring can be fabricated beams that connect the oscillators [9]. The governing equations are given by

$$\begin{aligned}
\dot{T}_1 + B_T T_1 - A_T P(1 + c_g z_1) = 0,\\
\ddot{z}_1 + \frac{(\dot{z}_1 - D\dot{T}_1)}{Q} + h_1(T_1)(z_1 - DT_1)\\
+3\sqrt{\frac{h_1(T_1)\beta}{2}}\tau(z_1 - DT_1)^2 + \beta(z_1 - DT_1)^3\\
= K(z_2 - z_1),\\
\dot{T}_2 + B_T T_2 - A_T P(1 + c_g z_2) = 0,\\
\ddot{z}_2 + \frac{(\dot{z}_2 - D\dot{T}_2)}{Q} + h_2(T_2)(z_2 - DT_2)\\
+3\sqrt{\frac{h_2(T_2)\beta}{2}}\tau(z_2 - DT_2)^2 + \beta(z_2 - DT_2)^3\\
= K(z_1 - z_2).
\end{aligned} \tag{6}$$

The spring acts a driving force that penalizes the difference between the two oscillators. The spring stiffness normalized by the linear stiffness of the oscillator ($K$ in eqnation 6) determines the ability of the two detuned oscillators to frequency lock. We integrate the system of equations 6 for different values of stiffness $K$ and detuning $\kappa$. We then detect frequency locking in the response of the two oscillators. The results are plotted in figure 7. When $\kappa = 1$ the two oscillators are identical and they do not need any spring for frequency locking. Figure 7 displays a linear relationship between the detuning and required stiffness of the spring. The required stiffness increases with detunung. At $\kappa = 0.9$, which corresponds to a frequency difference of $5\%$ between the oscillators, a coupling stiffness of $K \approx 1$ is required.

Fabrication of such arrays of devices is not easy and only nearest neighbor coupling can be achieved. To achieve global coupling between oscillators, we turn our attention to electrical coupling of oscillators.

## 4.2 Electrical Coupling

In the electrical form of coupling of the oscillators, the motion of one oscillator is converted to an electrical signa that is fed into the resistive heating of the other oscillator. Oscillator 2 thermally drives oscillator 1, without being affected by the dynamics of oscillator 1. The resulting model is given in equation 7. The term $\phi z_2$ corresponds to the driving seen by oscillator 1 due to the motion of oscillator 2. We now compute the regions where the response of oscillator 1 jumps onto its resonance curve. This region gives frequency locked behavior figure 8. Figure 8 shows that frequency locking is hysteretic with a narrow region in which entrainment is attained during both forward and negative frequency sweeps. The overall region of entrainment increases roughly linearly with the coupling strength $\phi$.

$$\begin{aligned}
\dot{T}_1 + B_T T_1 - A_T P(1 + c_g z_1 + \phi_c z_2)^2 = 0,\\
\ddot{z}_1 + \frac{(\dot{z}_1 - D\dot{T}_1)}{Q} + h_1(T_1)(z_1 - DT_1) +
\end{aligned}$$

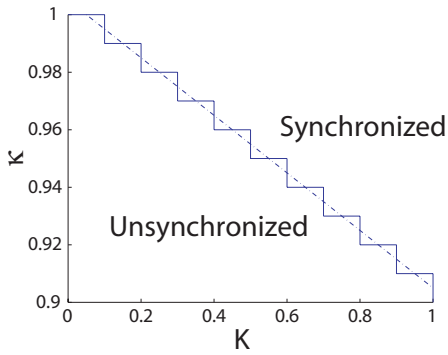


Figure 7: Region of frequency locking of two detuned oscillators with mechanical coupling.

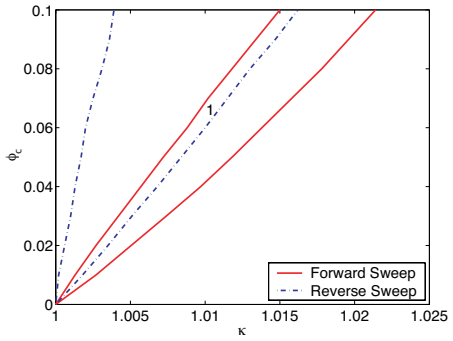


Figure 8: Region of frequency locking of two detuned oscillators with electrical coupling.

$$
\begin{aligned}
3\sqrt{\frac{h_1(T_1)\beta}{2}}\tau(z_1 - DT_1)^2 + \beta(z_1 - DT_1)^3 = 0,\\
\dot{T}_2 + B_T T_2 - A_T P(1 + c_g z_2)^2 = 0,
\end{aligned}
$$

$$
\begin{aligned}
\ddot{z}_2 + \frac{(\dot{z}_2 - D\dot{T}_2)}{Q} + h_2(T_2)(z_2 - DT_2) \quad +\\
3\sqrt{\frac{h_2(T_2)\beta}{2}}\tau(z_2 - DT_2)^2 + \beta(z_2 - DT_2)^3 \quad = \quad 0,
\end{aligned}
\tag{7}
$$

# 5 Conclusions

In this work we take the first steps to model a physical system that can eventually be used for filter applications, neurocomputing [2] or as a means of clock distribution. We select dome oscillators as an example and build a first principles model for the governing mechanical dynamics. Since the oscillator is thermally driven using a resistor, we also build a model for the governing thermal dynamics. A bifurcation analysis of the resulting ordinary differential equations is performed. Stable limit cycle oscillations of the dome oscillator are identified. Two oscillators are then mechanically and electrically coupled and the regions of synchrony are computed by changing the coupling parameter and detuning between the two oscillators.

# References

[1] R. Reichenbach et. al. *3rd Order Intermodulation in a Micromechanical Thermal Mixer*. J. Micromechanical Systems 14, 1244-1252, 2005.

[2] F. C. Hoppensteadt and E. M. Izhikevich. *Synchronization of MEMS Resonators and Mechanical Neurocomputing*. IEEE Trans. on Circuits and Systems - I, 48, 133-138, 2001.

[3] M. Zalalutdinov et. al. *Frequency entrainment for micromechanical oscillator*. Applied Physics Letters, 83, 3815-3817, 2003.

[4] Y. C. Fung. *Foundations of Solid Mechanics*. Prentice-Hall, 1965.

[5] S. P. Timoshenko and J. M. Gere, *Theory of Elasticity*. McGraw-Hill, 1961.

[6] S. Uma et. al. *Temperature-Dependent Thermal Conductivity of Undoped Polycrystalline Silicon layers*. International Journal of Thermophysics, 22, 605-616, 2001.

[7] W. N. Sharpe et. al. *Effect of specimen size on Young's modulus and fracture strength of Polysilicon*. Journal of Micromechanical Systems, 10, 317-326, 2001.

[8] J. Guckenheimer and P. Holmes. *Nonlinear Oscillations, Dynamical Systems and Bifurcations of Vector Fields*. Springer, 1996.

[9] M. Zalalutdinov et. al. *Two-dimensional array of coupled nanomechanical resonantors* Applied Physics Letters, 78,3142-3144, 2001. s

Proceedings of the 6th International Conference on
Computation of Shell and Spatial Structures
IASS-IACM 2008: "Spanning Nano to Mega"
28-31 May 2008, Cornell University, Ithaca, NY, USA
John F. ABEL and J. Robert COOKE (eds.)

# Fully Lagrangian dynamics of thin MEMS beam

Ranajay GHOSH*, Subrata MUKHERJEE

*220 Kimball Hall,
Cornell University,
Ithaca, NY 14853
rg248@cornell.edu

## Abstract

Micro-jets, micro-actuators and micro-speakers etc involve high frequency oscillations of thin beams or plate shaped conductors. Conventional Boundary Element Method (BEM) analysis of the electric field in a region exterior to such thin conductors can become difficult to carry out accurately and efficiently- especially since MEMS analysis requires computation of charge densities (and then surface traction) separately on the top and bottom surfaces of such beams. A new Boundary Integral Equation (BIE) is proposed to handle the computation of charge densities for such high aspect ratio geometries. In the current work, this has been coupled with Finite Element Method (FEM) to obtain the response behavior of devices made of such high aspect ratio structural members. In addition, almost all realistic systems are significantly influenced by the presence of fluid surrounding the device. This damping effect has been taken into account assuming very low Reynold's number Stokes flow around the beam. The Stokes flow is modeled using a conventional external boundary element method coupled in turn with the mechanical problem. This coupling of electrical, mechanical and fluid problem is carried out using a Newton scheme based on a Lagrangian description of the electrical ,mechanical and fluid domains. Numerical results are presented in this paper for the dynamic behavior of the coupled MEMS. The effect of gap between a beam and the ground, on mechanical response of a beam subjected to increasing electric potential, is studied carefully.

## 1. Introduction

The focus of this paper is the study of dynamic response of MEMS devices made up of very thin conducting beams. This requires BEM analysis of the electric field exterior to these thin conducting beams. A convenient way to model such a problem is to assume beams with vanishing thickness and solve for sum of the charges on the upper and lower surfaces of each beam (Harrington [2]). This paper is an attempt to analyze and simulate a practical MEM system like a microjet involving a coupling of the electro-mechanical problem with micro-fluidics. The external electric field is modeled using the Lagrangian version of the thin beam BEM approach (Mukherjee and Bao [4]) together with a hyper-singular post processing gradient BIE to find the individual charges. The mechanical problem is tackled using a moderately large deflection FEM analysis. The fluid modeled as a Stokes using a conventional external thin beam BEM analysis (Mukherjee et. al. [5]) using a corresponding Lagrangian version. Finally, a Newton scheme developed analogous to Aluru and De [1] is used to solve the entire coupled nonlinear problem. The paper starts with regularization of the conventional and hypersingular BIEs for the potential theory in an infinite region outside the thin conducting beams. The equations are then reformulated in a total Lagrangian framework. A finite element scheme is then presented for the mechanical deformation of the structure. The fluid is approximated as Stokes and a conventional BIE representing the fluid is then presented and the reformulated once again in a total Lagrangian framework. The paper then proceeds to explain the Newton scheme for coupling the electrical-mechanical-fluid domains.

## 2. Electrical problem in the exterior domain

The beam deforms when a potential V is applied between the two conductors, and the deformed configuration is called **b** with boundary ∂**b**. The charge redistributes on the surface of the deformed beam, thereby changing the electrical force on it and this causes the beam to deform further. As the deformation starts, the damping effects due to fluids come into play. The system then undergoes vibrations and the complete analysis of the system is done using the Newton scheme. The boundary integral formulation for the electric filed can be derived from the Laplace equation which governs the potential in the region outside a conductor.


Figure 1: Equivalent electrical system

*2.1 Conventional BIE – Indirect formulation*

Referring to Figure 1, for a source point $\xi \in$ B (without bounding surface ∂B), one has the indirect BIE,

$$\phi(\xi) = \int_{\partial B} -\frac{\log(r(\xi, y))}{2\pi\varepsilon} \nu(y) ds(y) \tag{1}$$

where **y** is a field point, φ is the potential, $r(\xi, y) = y - \xi$, $r = |r|$, $\varepsilon$ is the dielectric constant of the medium, *ds* is the area of an infinitesimal surface element on $\partial B$ and $\nu$ is the (unknown) surface density function on $\partial B$.

*2.2 Gradient BIE – Indirect formulation*

Taking the derivative of the potential - at the source point leads to an auxiliary hypersingular equation,

$$\nabla_\xi \phi(\xi) = \int_{\partial B} -\frac{\nu(y)}{2\pi\varepsilon} \nabla_\xi \log(r(\xi, y)) ds(y) = \int_{\partial B} \frac{\nu(y) r(\xi, y)}{2\pi r^2(\xi, y)\varepsilon} ds(y) \tag{2}$$

Note that, in general, the function $\nu(y)$ is not the charge density. It becomes equal to the charge density when **B** is the infinite region exterior to the conductors.

*2.3 BIEs in infinite region containing two thin conducting beams*

It has been shown by Bao & Mukherjee [4], that for this case,

$$\phi(x^+) = -\int_{s_1^+ - s_1} \frac{\log(r(x^+, y)\beta(y)}{2\pi\varepsilon} ds(y) - \int_{s_1} \frac{\log(r(x^+, y)\beta(y)}{2\pi\varepsilon} ds(y) - \int_{s_2^+} \frac{\log(r(x^+, y)\beta(y)}{2\pi\varepsilon} ds(y) \tag{3}$$

where $\beta(y) = \sigma(y^+) + \sigma(y^-)$, where $\sigma$ is now the charge density at a point on the beam surface. The second integral in Eq.(3) is logarithmically singular and the rest are regular except when the beam thickness and the gap become very small. Since β(y) is equal and opposite on the other two beams, another equation for $x^+ \in s_2^+$ will not give any additional information. A similar equation can be written down for the gradient version of the equation to obtain hyper-singular BIE for thin beams.

*2.4 Lagrangian formulation of the electrical problem*

The Lagrangian formulation is relatively straightforward and can be started using Nanson's Law,

$$nds = JN \bullet F^{-1} dS \quad (4)$$

where n and N are unit normal vectors to ∂b and ∂B, at the generic points **x** and **X,** respectively, $\mathbf{F} = \frac{\partial x}{\partial X}$ is the deformation gradient, $J = \det F$ and dS is an area element on ∂B. Here **X** and **x** denotes coordinates in the un-deformed and deformed configuration respectively. Eq. (4) is then used to effect a change of variables.

## 3. Mechanical problem in elastic beam

The beam is linearly elastic, has immovable ends and is of uniform cross section without any initial in-plane forces. The cross section is symmetric such that there is no twisting of the beam under applied bending moments. Also, u(x) is the axial deformation and w(x) the transverse displacement of the mid-line of the beam. The basic approach is to use the nonlinear strain-displacement equation in the energy expression and then derive equations of motion using Hamilton's principle.

*3.1 Finite element model for beams with immovable end*

The procedure followed here for FEM discretization of vibrating beams, is similar to standard methods(see, e.g., Zienkiewicz and Taylor [7]). However, in this particular problem the standard beam element needs a slight modification. This modification is necessitated because the usual linear interpolation for the axial deformation results in discontinuities during residue computation in the Newton's scheme. Now, the primary deformations **u, w** inside the elements can be interpolated from the above nodal values using, suitable interpolation functions. The final matrix equations are,

$$\begin{bmatrix} M^{(I)} & 0 \\ 0 & M^{(O)} \end{bmatrix} \cdot \begin{Bmatrix} \ddot{q}^{(I)}(t) \\ \ddot{q}^{(O)}(t) \end{Bmatrix} + \begin{bmatrix} K^{(I)} & 0 \\ 0 & K^{(O)} \end{bmatrix} \cdot \begin{Bmatrix} q^{(I)}(t) \\ q^{(O)}(t) \end{Bmatrix} + \begin{bmatrix} 0 & K^{(IO)} \\ 2K^{(IO)T} & 0 \end{bmatrix} \cdot \begin{Bmatrix} q^{(I)}(t) \\ q^{(O)}(t) \end{Bmatrix} = \begin{Bmatrix} P^{(I)}(t) \\ P^{(O)}(t) \end{Bmatrix} \quad (5)$$

where the in plane (I), out of plane(O) and coupled (IO) sub-matrices can be computed from the specific kind of interpolation used in the problem.

## 4. Damping problem in stokes fluid

MEMS plates and beams are typically tens to hundreds of micrometers long and with thickness in the order of micrometers (Roamn et. al. [6]). There exists a regime where due to the micrometer-scales involved, the Reynolds numbers of the surrounding flow are generally small enough, and natural frequencies low enough (in the range of 100 s of kiloHertz) to allow the use of a steady-state Stokes flow (sometimes called creeping flow) model. The other available model is the squeezed film damping model which has been investigated in detail before.

*4.1 BIE modeling of Stokes flow*

The governing equations for the Stokes flow are:

$$\nabla p(x) - \mu \nabla^2 v(x) = 0, \qquad \nabla \bullet v(x) = 0, \qquad x \in B \quad (6)$$

$$v(x) = g(x), \qquad x \in \partial B. \quad (7)$$

In the above v(x) stands for velocity, p(x) stands for pressure and μ is the dynamic viscosity of the fluid. B is the region *exterior* to the body.

*4.2 BIE in Stokes flow in infinite region around very thin beams*

It has been shown by Mukherjee et.al. [5] that for thin beam, the governing equations can be expressed in BIE form as,

$$v_i(x^+) = g_i(x^+) = \int_{s^+} T_{ij}(x^+, y) w_j(y) ds(y) + \int_{s^+} G_{ij}(x^+, y) q_j(y) ds(y), \quad x^+ \in s^+, \quad (8)$$

where $T_{ij}$ and $G_{ij}$ are respectively the velocity and traction kernel and $q_j = \tau_j^+ + \tau_j^-$ and $w_j = v_j^+ - v_j^-$ with $\tau$ and $v$ respectively the traction and velocity on the surfaces. For a very thin beam $v_j^+ \approx v_j^-$ which forces the first integral on the right hand side to vanish. We are thus left with a simplified version of Eq. (8),

$$v_i(x^+) = g_i(x^+) = \int_{s^+} G_{ij}(x^+, y) q_j(y) ds(y), \qquad x^+ \in s^+. \qquad (9)$$

For a 2D problem, the traction kernel has the form,

$$G_{ij} = \frac{1}{4\pi\mu}\left(-\delta_{ij} \log r + \frac{r_{,i} r_{,j}}{r^2}\right) \qquad (10)$$

The Lagrangian version of the Stokes BIE can be formulated using the same approach as the electrostatic problem starting from the Nanson's formula.

## 5. Implicit time integration for dynamic problem

Finally, time integration for the problem is implemented using the Newmark scheme utilizing Newton's scheme. The method follows closely from Liu et. al. [3]. The dynamic MEMS equation can be put in the following form,

$$M\ddot{U}(t) + KU(t) = F^{elec}(B(t)) + F^{flu}(\dot{U}(t)) \qquad (12)$$

Here, U is the displacement vector and dots indicate time derivatives. **M** and **K** are respectively the consistent mass matrix and stiffness matrix. $\mathbf{F^{elec}(B(t))}$ represents the electrostatic force which depends on the chargedistribution **B(t)** and $\mathbf{F^{flu}}$ represents the fluidic force vector which depends on the velocity distribution $\dot{U}(t)$. Eq. (12) can be solved using several direct integration methods when the fores are linear in displacement. However, many of these methods are not directly applicable to MEMS. Two methods applicable to MEMS analysis are the Central Difference Method and the Newmark Method. The algebraic domain equations are solved using Newton scheme and the Newmark method wraps around to march forward in time.

## References


[1] Aluru NR and De SK. Full-lagrangian schemes for dynamic analysis of electrostatic mems. IEEE J. Microelectromech. Syst., 13, 2004.

[2] Harrington RF. Field computation by Moment Methods. IEEE Press, 1993

[3] Liu WK Belytschko T and Moran B. Nonlinear Finite Element for Continua and Structures. John Wiley & Sons, Ltd., 2000.

[4] Mukherjee S and Bao Z. Electrostatic bem for mems with thin beams. Comm. Numer. Meth. Engng., 21:297–312, 2005.

[5] Mukherjee YX Mukherjee S and Telukunta S. Bem modeling of damping forces on mems with thin plates. Eng. Anal. Bound. Elem., 29:1000–1007, 2005.

[6] Roman M Bao Z, Mukherjee S and Aubry N. Nonlinear vibrations of beams, strings, plates and membranes without initial tension. ASME J. App. Mech., 71, 2003.

[7] Zienkiewicz OC and Taylor RL. The Finite Element Method, volume 1,2, 4th Ed. McGraw Hill, Berkshire,UK,2005.